Evaluation of AAV9 Mediated Gene Therapy in a Cranial Stochastic Postnatal Mouse Model of Tuberous Sclerosis Complex Type 2

A thesis submitted by

Niyoosha Abdollahpour

in partial fulfillment of the requirements for the degree of

Master of Science

in

Pharmacology and Drug Development

Tufts University

Graduate School of Biomedical Sciences

May 2026

Advisor: Chris Dulla, PhD

Abstract

Tuberous sclerosis complex (TSC) is a genetic neurodevelopmental disorder caused by loss-of-function mutations in TSC1 or TSC2, resulting in hyperactivation of the mechanistic target of rapamycin complex 1 (mTORC1) pathway. Neurological manifestations, particularly epilepsy, represent a major source of morbidity, and current therapies provide only partial or symptomatic relief without correcting the underlying genetic defect. Gene replacement therapy using adeno-associated virus (AAV) vectors has emerged as a potential disease-modifying strategy by restoring functional TSC protein expression, yet its efficacy in relevant disease models remain incompletely understood.

In this study, we characterized a stochastic cranial TSC2 knockout (scTSC2-KO) mouse model and evaluated the feasibility of AAV9-mediated delivery of condensed TSC2 construct (cTuberin). Neonatal mice received intracerebroventricular (ICV) AAV1-Cre to induce stochastic TSC2 deletion, followed by ICV administration of AAV9-cTuberin or control vector at postnatal day 21. Molecular and cellular phenotypes were assessed using immunohistochemistry and quantitative image analysis, while seizure activity was evaluated using chronic electrocorticography (ECoG).

We confirmed robust model validity, with TSC2-deficient neurons exhibiting significantly elevated phosphorylated S6 (pS6) levels and increased soma size, consistent with mTORC1 hyperactivation. Spatial analysis revealed region-dependent variability in recombination, with higher proportions of TSC2-deficient neurons primarily in hippocampus compared to cortical and subcortical regions.

In contrast, AAV9-mediated cTuberin delivery did not produce measurable improvements in seizure duration or frequency. Subsequent analysis revealed minimal detectable transgene expression, indicating limited viral transduction or expression efficiency under the conditions tested. These findings suggest that the lack of therapeutic effect is likely attributable to insufficient transgene delivery rather than ineffectiveness of the therapeutic construct itself.

Overall, this study establishes the scTSC2-KO model as a robust platform for investigating TSC2 pathophysiology and highlights key technical barriers to effective AAV-mediated gene replacement in the central nervous system. These results underscore the importance of optimizing vector design, dosing and delivery strategies to enable successful translation of gene therapy approaches for TSC.

Acknowledgements

I would like to express my deepest gratitude to my advisor, Dr. Chris Dulla, for his guidance, support, and mentorship throughout my graduate studies. His insight, patience, and encouragement were invaluable in shaping both this project and my development as a scientist. I am especially grateful for the opportunity to work in his lab and for his continuous support during both the successes and challenges of this research.

I would also like to sincerely thank my mentor, Dr. Zin Klaft, for his guidance, support and encouragement throughout this project. His mentorship, thoughtful feedback, and willingness to share his knowledge played a significant role in my learning and growth during this work.

I would like to thank my thesis reader, Dr. Leon Reijmers, for his time and his willingness to serve on my thesis committee.

I would like to thank the members of the Dulla Lab for their support, collaboration, and creating a welcoming and intellectually stimulating environment. I am particularly grateful to those who provided technical guidance, feedback, and assistance throughout this project. I extend my sincere thanks to our collaborators, including members of the Breakefield Laboratory at Massachusetts General Hospital, for their contributions to this work.

I am grateful to the faculty and staff of the Graduate School of Biomedical Sciences at Tufts University for their support and for providing a strong academic environment throughout my training. My sincere thanks also go to the Pharmacology and Drug Development Program, and its director, Dr. Emmanuel Pothos, for their support and time throughout my training.

Finally, I would like to express my deepest gratitude to my family and friends for their unconditional love and support. Their encouragement has been my greatest source of strength throughout my life and academic journey.

Table of Contents

Title Page i

Abstract ii

Acknowledgements iv

Table of Contents vi

List of Tables viii

List of Figures ix

List of Abbreviations: x

Chapter 1: Introduction 1

1.1 Background on Tuberous Sclerosis Complex 1
1.1.1 Genetics of TSC1/TSC2 1
1.1.2 mTORC1 pathway dysregulation 4
1.1.3 Neurological and Psychiatric Manifestations of TSC 6
1.1.4 Differences Between TSC2 and TSC1 Disease 9

1.2 Current TSC Therapeutic Strategies and Limitations 10
1.2.1 Rationale for Gene Replacement Approaches 15

1.3 AAV-Based Therapies 16
1.3.1 Overview of AAV Vectors for CNS Delivery 16

1.4 Stochastic TSC2-KO Mouse Model 20
1.4.1 Description of Model and Relevance 20
1.4.2 Advantages for Translational Studies 22

1.5 Study Objectives and Hypothesis 23
1.5.1 Primary Aims 23

Chapter 2: Materials and Methods 24

2.1 Stochastic, Cranial TSC2-KO Mouse Model 24

2.2 AAV Vector Design and Packaging 26

2.3 Immunohistochemistry 27
2.3.1 Image Acquisition 29

2.3.2 Quantification of mTORC1 Activity 30
2.3.3 Quantification of TSC2-KO Neuron Distribution 30
2.4 AAV9 Gene Therapy Injection Protocol 32
2.5 ECoG Implant Surgery 33
2.5.1 ECoG Recordings 34
2.6 Statistics 34

Chapter 3: Results 36

3.1 Validation of the Cranial Stochastic TSC2-KO Model 36
3.1.1 Quantifying mTORC1 Activity 36
3.1.2 Change in Neuronal Morphology 39
3.2 Regional Distribution of TSC2-KO Neurons Between Cortex and Hippocampus. 40
3.3 Distribution of TSC2-KO Neurons Across Smaller Brain Subregions 41
3.4. AAV9 Gene Therapy Study: In vivo ECoG Assessment of AAV9-Treated Mice 45
3.5 Assessment of Viral Transgene Expression 48
3.5.1 Viral Genome Integrity 50

Chapter 4: Discussion 51

4.1 Molecular mTORC1 activity and Neuronal Morphology 51
4.2 Distribution of TSC2-KO Neurons 53
4.3 Gene Therapy Study 55
4.4 Limitations 57
4.5 Future Directions 59

References 61

List of Tables

Table 2.3 Antibodies ……....28

List of Figures

Figure 2.1 Experimental design and stochastic TSC2 knockout mouse model ……25
Figure 2.2 Schematic representation of AAV9 vectors used for gene delivery ……26
Figure 3.1 Stochastic TSC2 deletion increases mTORC1 signaling and neuronal soma size in the somatosensory cortex ……...39
Figure 3.2 Distribution of TSC2-KO neurons in the somatosensory cortex and hippocampus ……42
Figure 3.3 Distribution of TSC2-KO neurons across multiple brain regions ……...45
Figure 3.4 In vivo ECoG analysis of seizure activity following AAV9-mediated gene delivery in scTSC2-KO mice ……48
Figure 3.5 Assessment of AAV9-mediated transgene expression following viral delivery……..….50

List of Abbreviations:

AAV: Adeno-associated virus
AAV1: Adeno-associated virus serotype 1
AAV9: Adeno-associated virus serotype 9
AC: Auditory cortex
ADHD: Attention deficit hyperactivity disorder
AP: Anteroposterior
ASD: Autism spectrum disorder
ASM: Anti-seizure medication
BSA: Bovine serum albumin
CA1: Cornu Ammonis region 1 of the hippocampus
CA3: Cornu Ammonis region 3 of the hippocampus
CNS: Central nervous system
Cre: Cre recombinase
cTub / cTuberin: Condensed tuberin construct
DAPI: 4′,6-diamidino-2-phenylindole
DG: Dentate gyrus
DV: Dorsoventral
ECoG: Electrocorticography
EF1α: Elongation factor 1-alpha promoter
EV: Empty vector
GAP: GTPase-activating protein
GFP: Green fluorescent protein
ICV: Intracerebroventricular
IHC: Immunohistochemistry
KO: Knockout
LAM: Lymphangioleiomyomatosis
LMM: Linear mixed-effects model
MC: Motor cortex
ML: Mediolateral
MRI: Magnetic resonance imaging
mTOR: Mechanistic target of rapamycin
mTORC1: Mechanistic target of rapamycin complex 1
NMI: No mutation identified
PBS: Phosphate-buffered saline
PFA: Paraformaldehyde
pS6: Phosphorylated ribosomal protein S6
REML: Restricted maximum likelihood
ROI: Region of interest
RSC: Retrosplenial cortex
RT: Room temperature
scTSC2-KO: Stochastic cranial TSC2 knockout mouse model
SEGA: Subependymal giant cell astrocytoma
SSC: Somatosensory cortex
TAND: TSC-associated neuropsychiatric disorders
TSC: Tuberous sclerosis complex

TSC1: Tuberous sclerosis complex gene 1 (hamartin)
TSC2: Tuberous sclerosis complex gene 2 (tuberin)
V5: V5 epitope tag
VNS: Vagus nerve stimulation
WT: Wild type

Chapter 1: Introduction

1.1 Background on Tuberous Sclerosis Complex

Tuberous sclerosis complex (TSC) is a multisystem neurodevelopmental disorder characterized by the development of benign hamartomatous lesions across multiple organs, including cortical tubers and subependymal nodules in the brain, renal angiomyolipomas, pulmonary lymphangioleiomyomatosis (LAM), cardiac rhabdomyomas, and various dermatological features (e.g., facial angiofibromas, hypomelanotic macules, shagreen patches). Aberrant growth of these lesions thus can lead to symptoms in multiple organ systems of TSC patients and clinical severity depends on degree and extent of TSC mutations. TSC exhibits significant phenotypic variability, with manifestations ranging from mild to life-threatening, and affects all ethnic groups and sexes equally (Northrup et al., 2021; Jurca et al., 2025; Kim SY, 2025). Epidemiological estimates indicate an incidence of approximately 1 in 6,000 to 1 in 10,000 live births, with prevalence ranging from 4-12.7 per 100,000 in the general population (Furber et al., 2025; Pentz et al., 2025; Jurca et al., 2025). Recent systematic reviews conform a stable but potentially underdiagnosed prevalence as higher rates are often observed in cohorts when using updated diagnostic criteria that include more readily available genetic confirmation (Furber et al., 2025; Kim SY, 2025).

1.1.1 Genetics of TSC1/TSC2

Clinical manifestations of TSC are caused by loss of function mutations in either TSC1 (chromosome 9, encoding hamartin) or TSC2 (chromosome 16, encoding tuberin).

Pathogenic variants follow an autosomal dominant inheritance pattern with high penetrance, though phenotypic variability is pronounced even within families. Approximately 60-70% of TSC cases arise from *de novo* (sporadic) mutations, with the remainder inherited from an affected parent (Northrup et al., 2024; Chen et al., 2025). Recent large cohorts and diagnostic studies confirm that TSC2 mutations predominate, accounting for ~65-75% of identified pathogenic variants, while TSC1 mutations represent ~20-30%; the remaining ~5-15% are classified as "no mutation identified" (NMI) despite comprehensive testing (Northrup et al., 2024; Chen et al., 2025; Praticò et al., 2025). NMI cases may result from technical limitations in detection (e.g., deep intronic variants, complex rearrangements), or low-level somatic mosaicism, which may be missed in blood-based testing and sometimes requires analysis of additional tissues for detection.

The pathogenesis is thought to follow a mechanism similar to Knudson's classic "two-hit" tumor suppressor model (Knudson, 1971): a germline mutation (inherited or *de novo*) inactivates one allele in all cells, rendering them haploinsufficient, while a subsequent somatic "second hit" (often loss of heterozygosity, point mutation, or deletion) eliminates the remaining wild-type allele in specific cell lineages. This biallelic inactivation drives focal, mosaic hamartoma formation across organs (Thiele et al., 2010; Cheah et al., 2021; Dufner-Almeida et al., 2024; Chen et al., 2025). Second hits are well-documented in peripheral tumors (e.g., renal angiomyolipomas, SEGAs), but less consistently in cortical tubers, where haploinsufficiency alone or alternative mechanisms (e.g., epigenetic dysregulation) may suffice for pathology (Martin et al., 2017; Kashii et al., 2023).

Importantly, while biallelic inactivation drives focal hamartoma formation, germline haploinsufficiency alone appears sufficient to contribute to neurological dysfunction, as evidenced by the diffuse neurological features observed in TSC patients including epilepsy, intellectual disability, autism spectrum features, and TAND, manifestations that are not strictly limited to tissues with documented second hits (Martin et al., 2017; Mizuguchi et al., 2021). The degree to which these clinical manifestations emerge is further shaped by the mutational mechanism underlying each case.

Mosaicism in TSC can arise through two distinct mechanisms that have importantly different clinical implications. In the classical two-hit scenario described above, the first hit is present in every cell, and mosaicism emerges focally through somatic second-hit events in specific cell lineages, driving discrete hamartoma formation. In a second scenario, the first-hit variant itself arises post-zygotically, producing first-hit mosaicism where only a subset of cells across the body carries the pathogenic allele. This distinction matters clinically: individuals with first hit mosaicism have a fundamentally restricted pool of cells capable of undergoing second-hit loss, which typically results in lower variant allele fractions detectable in blood, frequent diagnostic under-detection, and generally milder or more localized disease burden compared to those with a constitutional first hit. This likely accounts for a meaningful proportion of NMI cases mentioned above, where standard blood-based testing fails to detect the variant. Nevertheless, severity in mosaic-first-hit cases remains dependent on the developmental timing of the mutation and the tissue distribution of affected cells, and severe phenotypes are not precluded (Giannikou et al., 2019; Ogórek et al., 2020; Klonowska et al., 2023).

Independently of mosaicism, mutation spectra differ between genes. TSC1 variants are predominantly truncating (nonsense, frameshift, small insertions/deletions), with missense mutations being rare (<5%). TSC2 variants are more diverse, including frequent missense changes, large deletions/rearrangements, and splice-site alterations (Rosengren et al., 2020; Chen et al., 2025; Praticò et al., 2025). Over 6,000 unique variants have been cataloged, with TSC2 showing higher mutational burden. These differences contribute to clinical heterogeneity and severity. TSC2 pathogenic variants are associated with more severe phenotypes overall, including earlier seizure manifestation compared to TSC1 (Dabora et al., 2001; Jansen et al., 2008; Kashii et al., 2023; Chen et al., 2025; Praticò et al., 2025).

1.1.2 mTORC1 pathway dysregulation

The TSC1 (hamartin) and TSC2 (tuberin) proteins form a stable heterodimeric complex that acts as a critical negative regulator of the mechanistic target of rapamycin complex 1 (mTORC1) pathway. Specifically, the TSC complex functions as a GTPase-activating protein (GAP) for the small GTPase Rheb, accelerating the hydrolysis of Rheb-GTP to Rheb-GDP and thereby inhibiting mTORC1 activation at the lysosomal surface (Kwiatkowski & Manning, 2005; Laplante & Sabatini, 2012). Under physiological conditions, this inhibition maintains cellular homeostasis by balancing anabolic processes (e.g., protein synthesis via S6K/4E-BP1, ribosome biogenesis, lipid and nucleotide production) with catabolic ones (e.g., suppression of autophagy via ULK1 inhibition). Loss-of-function mutations in TSC1 or TSC2 disrupt complex stability and GAP activity, leading to unchecked Rheb-GTP accumulation and constitutive mTORC1 hyperactivation

(Chen et al., 2025; Kim SY, 2025). This drives aberrant cell growth, proliferation, and metabolic reprogramming, while suppressing autophagy and altering cellular stress responses. In the central nervous system (CNS), mTORC1 dysregulation has profound neurodevelopmental consequences: it impairs neuronal migration and differentiation, disrupts cortical layering, promotes abnormal synaptogenesis and dendritic spine density, induces neuroinflammation, and enhances neuronal excitability through altered ion channel expression and synaptic plasticity (Kim SY, 2025; Afshar-Saber et al., 2025; Chen CS, 2025).

Recent studies using human iPSC-derived neuronal models of TSC suggest that dysregulated mTORC1 signaling during neuronal maturation can alter activity-dependent transcriptional programs. In TSC2-deficient excitatory neurons, reduced expression of the immediate-early transcription factor EGR1, which is normally induced by neuronal activity and regulates genes involved in synaptic plasticity, has been reported together with impaired activity-dependent gene expression and abnormalities in maturation-associated DNA methylation dynamics (Ercan, Han et al. 2017). These findings raise the possibility that early mTORC1 hyperactivation may initiate persistent transcriptional and epigenetic changes during neuronal development, potentially limiting the ability of later mTORC1 inhibition to fully normalize neuronal activity or gene expression.

Consistent with this idea, experimental studies using TSC2 mutant human iPSC-derived neurons have demonstrated altered neuronal maturation, dysregulated network activity, radial migration abnormalities, and transcriptional abnormalities linked to mTORC1 hyperactivation (Winden et al., 2019; Chen et al., 2025; Kim SY, 2025). In addition to

transcriptional effects, mTORC1 dysregulation suppresses autophagy and promotes excessive protein synthesis, which can contribute to neuronal hypertrophy, abnormal cortical organization, and the formation of cortical tubers observed in TSC neuropathology (Bateup, Johnson et al. 2013, Caban, Khan et al. 2017). Together, these CNS specific consequences of mTORC1 hyperactivation contribute to the major neurological manifestations of TSC, expressing heterogeneous epilepsy phenotype and TSC associated neuropsychiatric disorders (TAND, e.g., ASD, intellectual disability), highlighting mTORC1 as a convergent pathogenic hub amenable to targeted therapies.

1.1.3 Neurological and Psychiatric Manifestations of TSC

Neurological symptoms are the predominant source of morbidity and reduced quality of life in TSC, with epilepsy representing the most frequent and debilitating manifestation. Recent systematic reviews and large cohort studies report epilepsy prevalence ranging from 60-90% overall, with rates often higher in pediatric populations (typically 80-90%, and up to 93% in some series) compared to adults (around 64% on average, though with wide variability due to ascertainment and survival bias) (Lindsay et al., 2024; Furber et al., 2025; Jurca et al., 2025; Kim SY, 2025; Osman et al., 2025). Seizures commonly emerge early in life, with onset in the first year in the majority of cases; infantile spasms (often evolving into or co-occurring with focal seizures) affect a median of ~47% of patients with TSC (range 1.7–74% across studies), while focal seizures and generalized seizures that frequently emerge later in childhood or persist into adulthood (Nabbout et al., 2018; de Saint Martin et al., 2022; Furber et al., 2025).

Early epileptogenesis during critical periods of cortical development, driven by mTORC1 hyperactivation, disrupted neuronal migration, abnormal synaptogenesis, and cortical dysplasia (including tubers), profoundly impairs network maturation and connectivity. This leads to high rates of drug-resistant (refractory) epilepsy in 45-85% of cases (higher in children and those with infantile spasms history), persistent breakthrough seizures despite multiple therapies, increased risk of status epilepticus, and elevated mortality (Furber et al., 2025; Pentz et al., 2025; Toscano-Prat et al., 2025). Sudden unexpected death in epilepsy (SUDEP) is a major concern, contributing significantly to TSC-related mortality (up to 25% of epilepsy-attributable deaths in some studies), alongside status epilepticus and seizure-related complications. Overall, TSC patients with epilepsy face a 4.3-fold higher mortality risk compared to those without seizures or the general population, with 1.4% - 13.8% mortality rate per 100 individuals (over 11-45 years), along with reduced life expectancy (Pentz et al., 2025; Furber et al., 2025; Parthasarathy et al., 2021). Epilepsy-related deaths often stem from uncontrolled seizures, while non-epilepsy causes (e.g., renal failure, SEGA, LAM) predominate in long-term survivors.

Beyond epilepsy, TSC-associated neuropsychiatric disorders (TAND) represent a broad spectrum of cognitive, behavioral, and psychiatric comorbidities that significantly compound the neuropsychiatric burden. TAND affects up to 90% of individuals with TSC over their lifetime and includes autism spectrum disorder (ASD; prevalence 25–63%, often 40–50% in recent cohorts), intellectual disability (50–68%), attention deficit/hyperactivity disorder (ADHD; 30–50%), anxiety and depressive disorders (30–60%), as well as sleep disturbances, and adaptive functioning deficits (de Vries et al., 2015; de Vries et al., 2020; Furber et al., 2025; Kim SY, 2025; Osman et al., 2025).

Early-onset and refractory epilepsy, particularly infantile spasms, is strongly correlated with worse TAND outcomes, including higher ASD rates (52% in children with a history of infantile spasms versus 26% in those without infantile spasms), more severe intellectual disability, and greater behavioral impairment, likely due to shared pathogenic mechanisms (e.g., disrupted early brain development and chronic network hyperexcitability) (Mitchell, Mitchell et al. 2022, Lindsay, Runicles et al. 2024, Osman, Hadid et al. 2024, Furber, Martin et al. 2025). These comorbidities impose substantial psychosocial and economic burdens, severely impacting patient independence, caregiver quality of life, family dynamics, educational/occupational attainment, and increase healthcare utilization due to more hospitalizations, specialist visits, and indirect costs (Furber et al., 2025).

The close relation between epilepsy and TAND underscores the need for early seizure management. Importantly, early diagnosis of TSC is often possible prenatally or in the neonatal period due to the presence of cardiac rhabdomyomas detectable by fetal or early-life echocardiography, enabling identification of high-risk infants even before neurological symptoms emerge. This early window of detection has enabled preventative strategies, as pre-symptomatic vigabatrin in high-risk infants has been shown to improve neurodevelopmental outcomes, emphasizing the existence of a critical developmental window. This is particularly important given that uncontrolled seizures are strongly associated with more severe cognitive and psychiatric impairments (Cusmai, Moavero et al. 2011, Moavero, Benvenuto et al. 2019, Jozwiak, Kotulska et al. 2020). Despite advances, refractory epilepsy and TAND remain major unmet needs, driving research into disease-modifying therapies like gene replacement.

1.1.4 Differences Between TSC2 and TSC1 Disease

Pathogenic variants in TSC2 are more common than those in TSC1, accounting for approximately 65-85% of identified mutations in large patient cohorts analyzed using comprehensive sequencing and copy number approaches (Dabora et al., 2001; Ogórek et al., 2020; Dufner-Almeida et al., 2024). In comparison, TSC1 variants represent roughly 15-35% of cases. Importantly, patients with TSC2 pathogenic variants consistently exhibit more severe clinical phenotypes than those with TSC1 variants.

In a landmark cohort of 224 patients studied, sporadic cases with TSC2 mutations demonstrated significantly higher frequencies of seizures, greater numbers of cortical tubers and subependymal nodules, more moderate to severe intellectual disability, and more extensive renal involvement (including angiomyolipoma and cysts) compared with age-matched TSC1 cases. Retinal hamartomas and liver angiomyolipomas were virtually absent in TSC1 patients but present in TSC2 patients (Dabora et al., 2001).

These findings are further supported by prospective infant studies. In the EPISTOP study (94 infants with TSC followed to age 2 years), TSC2 mutations accounted for approximately 75% of mutation-positive cases and were associated with more severe clinical presentation. Infants with TSC2 mutations exhibited a significantly higher cortical tuber burden (median tuber count ~24 in TSC2 versus ~8 in TSC1), earlier seizure onset (median ~4-5 months in TSC2 versus 8-10 months in TSC1), and increased risk of drug-resistant epilepsy. Additionally, TSC2 mutations were associated with higher prevalence of developmental delay, facial angiofibromas, renal cysts, and SEGA, with shorter seizure-free survival compared to TSC1(Ogórek et al., 2020). Experimental

evidence further supports these clinical findings: neuron-specific conditional knockout mouse models show that loss of TSC2 results in more severe social deficits and autism-like behaviors than equivalent TSC1 inactivation (Kashii et al., 2023).

Despite this general pattern, exceptions exist. Low-level mosaic variants and hypomorphic alleles in either gene can result in milder or incomplete phenotypes, even in cases involving TSC2 (Rosengren et al., 2020; Tian et al., 2021; Klonowska et al., 2023). Overall, TSC2 mutations are both more prevalent and more strongly associated with severe neurological and systemic manifestations, including earlier seizure onset, greater pharmacoresistance, increased cortical tuber burden, and higher risk of intellectual disability and autism spectrum disorder. These trends are further supported by animal models demonstrating more pronounced neurological dysfunction following TSC2 loss (Zeng et al., 2011).

1.2 Current TSC Therapeutic Strategies and Limitations

Management of TSC is multifaceted and multidisciplinary, encompassing both symptomatic treatments and mechanism-based therapies. While many interventions focus on controlling seizures, tumor growth, and associated complications, including TAND, targeted treatments such as mTOR inhibitors (e.g., everolimus and sirolimus) aim to address the underlying dysregulation of the mTOR pathway and modify disease progression. Epilepsy treatment follows a stepwise approach, prioritizing early intervention to mitigate developmental impacts. According to updated guidelines from the International TSC Consensus Group and recent reviews, first-line therapy for TSC-associated infantile spasms and early-onset focal seizures is vigabatrin. This treatment is

highly effective (response rates >80% in infantile spasms) when initiated promptly, often even pre-symptomatically upon detection of epileptiform EEG abnormalities (Northrup et al., 2021; Specchio et al., 2023; Valente et al., 2025).

Vigabatrin acts by inhibiting GABA metabolism via GABA transaminase, enhancing inhibitory neurotransmission, and is recommended as early as possible to reduce epilepsy severity and associated cognitive risks (Specchio et al., 2023; Debopam S., 2024). However, its main limitation is the risk of irreversible peripheral visual field defects, reported in approximately 15-31% of infants and young children with long-term exposure. Although lower rates of clinically confirmed renal toxicity (~0.7%) have been reported in systematically monitored pediatric TSC cohorts, this adverse effect remains a significant concern (Jonsson et al., 2022).

For focal, multifocal and generalized seizure types, conventional anti-seizure medications (ASMs) such as levetiracetam, valproate, lamotrigine, topiramate, oxcarbazepine, zonisamide, lacosamide, perampanel, and brivaracetam serve as mainstay therapies, often in polytherapy regimens (Valente et al., 2025; Conte et al., 2024). However, pharmacoresistance develops in approximately 50-70% of TSC patients, even with optimized treatment regimens. This reflects the fact that conventional ASMs provide symptomatic seizure control without targeting the underlying mTORC1 driven disease pathology. As a result, cumulative side effects associated with polytherapy, including cognitive slowing, behavioral disturbances, and sedation, are common, particularly in young children, and contribute to long-term developmental burden (Chu-Shore et al., 2010; Ogórek et al., 2020).

In pharmacoresistant cases, additional pharmacological and non-pharmacological interventions are considered as part of a comprehensive epilepsy management strategy. Cannabidiol (purified oral formulation, Epidiolex) received FDA and EMA approval in 2021 as adjunctive treatment for TSC-associated seizures (age ≥ 2 years), with randomized trials demonstrating significant seizure frequency reductions (median ~48-50% versus placebo) and overall good tolerability (Specchio et al., 2023; Valente et al., 2025). Its mechanism may involve modulation of mTOR signaling and anti-inflammatory pathways. However, adverse effects, including somnolence, decreased appetite, diarrhea, and elevated liver enzymes, lead to permanent discontinuation in 6-14% of patients, and long-term seizure freedom rates remain low (Thiele et al., 2021; Wu et al., 2024).

Non-pharmacological approaches are also important in refractory cases. The ketogenic diet (high-fat, low-carbohydrate) reduces seizure in approximately 30-50% of TSC patients, particularly in infants and young children, potentially through metabolic shifts influencing mTOR (Conte et al., 2024; Valente et al., 2025). However, long-term adherence is limited by dietary restrictiveness, gastrointestinal side effects (constipation, vomiting), nutritional deficiencies (dyslipidemia, kidney stones), and growth concerns. Sustained efficacy is also variable, with only 19-32% of patients maintaining >50% seizure reduction at 21 months (Park et al., 2017; Fang et al., 2022). For patients who are not candidates for resective surgery, vagus nerve stimulation (VNS) can offer modest seizure reduction by approximately 25-50%. However, seizure freedom is uncommon (<20%), response is often delayed (typically 6-12 months or longer), and efficacy tends to plateau over time. Common side effects include hoarseness, cough, dyspnea on

exertion, and rarely implant complications like infections or lead fractures occur (Englot et al., 2016; Toffa et al., 2020).

In selected patients with identifiable epileptogenic tubers, epilepsy surgery, including tuberectomy, focal resection, or laser interstitial thermal therapy, can be highly effective, achieving seizure freedom in approximately 50-70% of pediatric cases when performed early (Specchio et al., 2023; Singh et al., 2023; Hale et al., 2025). However, only a minority (~13%) of TSC patients with drug-resistant epilepsy ultimately undergo surgery due to multifocal or bilateral tubers. Long-term outcomes also show declining seizure freedom rates (~41% at a mean follow-up 6.8 years), and there is some risk involved with incomplete resection leading to reduced efficacy (Hale et al., 2025; real-world US cohort). Current guidelines strongly recommend early surgical evaluation for drug-resistant epilepsy to optimize neurodevelopmental outcomes (Northrup et al., 2021; Specchio et al., 2023).

In contrast to these primarily symptomatic and palliative approaches, mTOR inhibitors represent a mechanism-based therapeutic strategy targeting the underlying disease biology. Everolimus is approved by both the FDA and EMA as adjunctive therapy for refractory TSC-associated focal seizure (age ≥ 2 years), based on results from the phase 3 EXIST-3 trial. This study demonstrated ≥ 50% seizure reduction in approximately 40% of patients receiving high-exposure everolimus compared to 15% in the placebo group, with median seizure frequency reduction of up to ~40% (French et al., 2016).

Sustained therapeutic benefit has been demonstrated in open-label extension studies (long-term follow-up phases following completion of the initial clinical trial), with

responder rates increasing over time (e.g., 57.7% at 2 years in open-label extensions) and median seizure frequency reductions of 47-57%, alongside a generally tolerable safety profile (stomatitis, infections, hyperlipidemia as the main adverse effects) (Davis et al., 2017; Nabbout et al., 2018; Franz et al., 2021). In addition to seizure control, everolimus also provides tumor control (SEGAs, renal angiomyolipomas, LAM) and potential neurodevelopmental benefits when started early, though optimal timing and long-term CNS effects require further study (Specchio et al., 2025). Ongoing trials like TSC-STEPS [NCT05104983] and ViRap [NCT04987463] are evaluating preventive sirolimus or vigabatrin vs. rapamycin in infants, with results anticipated by late 2026.

While mTOR inhibitors provide meaningful adjunctive seizure control and systemic benefits, limitations persist. Complete seizure freedom is rarely achieved, even with optimized therapy, reflecting the high prevalence of drug-resistant epilepsy in TSC. Treatment responses vary by exposure level, patient age, and baseline severity (Franz et al., 2021; Specchio et al., 2025). Side effects (e.g., stomatitis, infections, immunosuppression, growth impacts) necessitate monitoring and may limit lifelong use, especially in pediatrics. Although this therapeutic approach is not fully restorative, mTOR inhibitors partially suppress mTORC1 but importantly do not correct the underlying TSC1/TSC2 loss, leaving residual pathology (e.g., established tubers, network hyperexcitability) and incomplete prevention of epileptogenesis or TAND progression (Conte et al., 2024; Becker et al., 2025).

1.2.1 Rationale for Gene Replacement Approaches

TSC is a monogenic disorder making it an ideal candidate for gene replacement therapy opening the possibility for causal treatment. By delivering a functional copy of the deficient gene (TSC2 or TSC1), this approach restores the TSC1/TSC2 protein complex, thereby normalizing mTORC1 signaling at its source rather than partially inhibiting downstream hyperactivation as achieved with rapalogs (everolimus/sirolimus). This approach could offer more comprehensive and durable benefits, including prevention of epileptogenesis during critical developmental windows, and improved neurodevelopmental outcomes, potentially with a single administration rather than lifelong daily dosing (Cheah et al., 2021; Prabhakar et al., 2019; Chen et al., 2025).

Importantly, TSC is particularly well suited for gene replacement strategies because excessive expression of either protein is unlikely to produce toxic gain-of-function effects. The TSC proteins hamartin and tuberin function as an obligate heterodimer, and hamartin stabilizes tuberin by preventing its ubiquitination and proteasomal degradation, indicating that the two proteins are interdependent for stability (Benvenuto et al., 2000; Chong-Kopera et al., 2006). As a result, protein subunits that fail to assemble into the TSC complex are typically unstable and degraded intracellularly, limiting the likelihood that excess protein would accumulate to pathogenic levels. These biochemical properties reduce a common concern in gene therapy, harmful overexpression of the therapeutic protein, and support the feasibility of restoring TSC complex function through gene replacement.

In contrast, current common therapeutic approaches targeting mTOR primarily provide symptomatic relief but fail to fully correct the underlying genetic defect. Clinical trials of mTOR inhibitors demonstrate meaningful seizure reductions and tumor control in many patients but fail to achieve complete seizure control in a substantial proportion of individuals, and treatment often requires lifelong administration with risks of chronic adverse effects including stomatitis, infections, metabolic disturbances, and immunosuppression (French et al., 2016; Franz et al., 2021). Persistent pathway dysregulation may also contribute to incomplete regression of established lesions and ongoing neurodevelopmental abnormalities. By restoring the upstream regulatory complex, gene replacement therapy has the potential to provide durable pathway normalization in post-mitotic cells such as neurons, potentially preventing epileptogenesis during critical developmental windows and limiting mosaic lesion formation driven by somatic second-hit events. If successful, this strategy could offer long-lasting therapeutic benefit following a single administration rather than lifelong pharmacologic inhibition of mTOR signaling.

1.3 AAV-Based Therapies

1.3.1 Overview of AAV Vectors for CNS Delivery

Adeno-associated virus (AAV) vectors have emerged as one of the most widely used platforms for gene delivery to the central nervous system (CNS), owing to their low immunogenicity, ability to transduce post-mitotic cells such as neurons, and capacity for long-term episomal expression in non-dividing tissues (Foust, Nurre et al. 2009, Deverman, Pravdo et al. 2016, Chan, Jang et al. 2017). However, a major challenge for

systemic gene therapy targeting neurological diseases is the blood-brain barrier (BBB), which restricts the passage of most circulating macromolecules into the CNS. Consequently, efficient CNS gene therapy often requires viral vectors capable of crossing the BBB following systemic administration.

Among naturally occurring serotypes, AAV9 has demonstrated the ability to cross the BBB after intravenous injection and achieve widespread neuronal and glial transduction in rodents and non-human primates (Foust, Nurre et al. 2009). These properties have enabled systemic gene delivery approaches in several neurological disease models and underlie the clinical success of AAV9-based therapies. Most notably, onasemnogene abeparvovec (Zolgensma), an AAV9 vector delivering a functional SMN1 transgene, was first systemically administered AAV gene therapy approved by the FDA and EMA for spinal muscular atrophy type 1. Pivotal trials demonstrated dramatic improvements in motor function, milestone achievement, and survival after a single intravenous infusion in infants (Mendell, Al-Zaidy et al. 2017). Nevertheless, the efficiency of AAV9-mediated BBB transduction varies across species, developmental stages, and disease states, and achieving robust, brain-wide gene delivery in adults remains a significant challenge.

Despite these encouraging advances, systemic AAV gene therapy has also revealed important safety considerations that continue to shape clinical development. Notably, a high-dose systemic AAV9 clinical trial for X-linked myotubular myopathy reported several patient deaths associated with severe liver dysfunction following vector administration, highlighting potential risks related to immune responses, vector dose, and off-target organ toxicity (Hinderer, Katz et al. 2018).

Nonetheless, these safety concerns must be weighed against the profound therapeutic potential of AAV-based gene replacement for severe genetic disorders that currently lack effective treatments. For devastating, life-threatening conditions such as tuberous sclerosis complex, where patients can experience refractory epilepsy, progressive neurological impairment, and multi-organ pathology, gene therapy offers the possibility of disease modification rather than symptomatic management. Advances in vector engineering have enabled the exploration of AAV9-mediated gene replacement strategies and alternative capsids for gene delivery in TSC patients. Proof-of-concept preclinical studies in mouse models have demonstrated striking efficacy of AAV9-mediated TSC gene replacement. In stochastic TSC1 floxed cerebral mouse models, postnatal intravenous delivery of AAV9 encoding full-length hamartin significantly reduced ependymal and subependymal brain lesions, normalized cell proliferation and mTORC1 signaling (including reduced phosphorylation of the downstream target S6), improved neurological phenotypes, and markedly extended survival when administered at postnatal day 21 (Prabhakar et al., 2019; Abou Haidar et al., 2025).

Similar therapeutic benefits have been observed in TSC2-deficient models, despite the large size of the TSC2 coding sequence, which is above the packaging limit of AAV9 vectors. To overcome this limitation, collaborators from the Breakefield Lab (MGH) engineered condensed forms of tuberin (cTuberin) that retain key functional domains while fitting within AAV packaging constraints. Systemic delivery of AAV9-cTuberin in CNS-specific TSC2 knockout mice resulted in normalization of mTOR signaling, reduction of ependymal lesions, prevention of hydrocephalus, and substantial extension of lifespan (Cheah et al., 2021). These findings demonstrate that even partial restoration

of TSC complex activity can significantly modify disease progression in vivo. However, anticonvulsant efficacy of this therapeutic approach has not been assessed yet.

Beyond CNS pathology, systemic AAV delivery offers the potential for multi-organ therapeutic coverage, which is particularly relevant for TSC given the widespread involvement of tissues such as kidney (angiomyolipomas), lung (lymphangioleiomyomatosis), and skin. Importantly, long-term transgene expression in post-mitotic cells such as neurons raises the possibility that a single administration could provide durable therapeutic benefit, potentially interrupting disease progression during critical developmental windows when mTOR dysregulation drives abnormal neurodevelopmental trajectories.

Recent translational developments further support the feasibility of this approach. Advances in next-generation capsid engineering, including receptor-targeted vectors increasing target specificity as well as other BBB-penetrant vectors, aim to improve brain delivery while minimizing off-target peripheral transduction. In parallel, regulatory agencies such as the FDA have begun to define and offer streamlined preclinical development pathways for AAV-based TSC gene therapy programs. Collectively, these efforts provide a strong foundation for evaluating AAV-mediated TSC2 replacement in disease models, such as stochastic TSC2-knockout mice, with the goal of assessing impacts on *in vivo* seizure burden, lesion formation, and neurobehavioral outcomes.

Despite the demonstrated ability of AAV9 to cross the BBB following intravenous administration, AAV9 vectors can also be delivered directly into the central nervous system via intracranial routes, including intracerebroventricular (ICV), intraparenchymal,

or intrathecal injection. Direct CNS administration bypasses the BBB, allowing for lower vector doses, reduced peripheral organ exposure, and more spatially controlled transduction within targeted brain regions. Intracerebroventricular delivery has been shown in research studies to achieve robust transduction of periventricular and cortical regions in neonatal and juvenile mice (Foust et al., 2009). Each delivery route presents distinct translational considerations. Systemic administration offers the advantage of multi-organ coverage, which is particularly relevant for disorders such as TSC. Intracranial delivery enables direct CNS targeting while minimizing systemic vector burden, thereby allowing clearer integration of CNS-specific therapeutic effects in preclinical models.

In the presented study, we opted for ICV delivery of AAV9-cTuberin at postnatal day 21 for this initial cohort of animals. This approach was selected to (I) ensure robust and localized CNS transduction, (II) reduce confounding peripheral effects, and (III) directly evaluate the capacity of cTuberin to rescue neuronal and network-level phenotypes within the brain. Future studies will directly compare intracranial and systemic delivery routes to determine their relative efficacy, safety, and translational potential in the stochastic TSC2-KO model.

1.4 Stochastic TSC2-KO Mouse Model

1.4.1 Description of Model and Relevance

The stochastic cranial TSC2 knockout (scTSC2-KO) mouse model was developed to recapitulate the “second-hit” somatic mutations that drive focal brain lesions in human TSC. In this model, homozygous TSC2-floxed ($TSC2^{fl/fl}$) mice carrying the Ai9 Cre-

dependent tdTomato reporter allele receive bilateral intracerebroventricular (ICV) injection of AAV1-CBA-Cre (1×10^{12} vg/kg) at postnatal day 0 (P0). Cre recombinase induces stochastic recombination of the floxed TSC2 alleles, resulting in deletion of both TSC2 copies in a stochastic manner across the brain. This approach therefore results in two types of cells within the same brain, TSC2-KO cells that are infected and uninfected cells that will remain wild type in regard to TSC2, producing heterogeneity and therefore mimicking key aspects of clinical TSC2 presentations.

The scTSC2-KO model exhibits several neuropathological features consistent with human TSC, including subependymal nodules, increased mTORC1 signaling (elevated phosphorylated-S6 levels), abnormal cell proliferation, ventriculomegaly, and progressive hydrocephalus. Untreated scTSC2-KO mice exhibit a median survival of approximately 58 days (Cheah, Prabhakar et al. 2021). Previous unpublished electrophysiological recordings from the Dulla lab confirm spontaneous convulsive electrographic seizures >80% of animals (average ~7 seizures per day, each lasting ~40 seconds) and abundant high-amplitude abnormal activity occupying ~50% of recording time.

This stochastic approach was adapted from earlier TSC1 models (Prabhakar, Goto et al. 2013) to specifically address TSC2 loss, which is associated with more severe clinical phenotypes. Importantly, the scTSC2 model is locally restricted to the brain. This local approach avoids potentially lethal and non-CNS involvement resulting in sufficiently long survival enabling the study of CNS-mediated symptoms of TSC such as seizures and TAND. In contrast, germline or ubiquitous knockout models either exhibit embryonic lethality or develop severe early phenotypes that limit their utility for therapeutic studies. Although mouse models generally do not develop cortical tubers, as seen in human

patients, the scTSC2-KO model still provides a highly relevant experimental platform. It enables investigation of disease mechanisms and evaluation of therapeutic strategies across multiple levels of analysis, including cellular pathology, dysregulation of mTORC1 signaling pathway, and network-level dysfunction such as spontaneous seizure activity. Consequently, this model offers a clinically relevant system for evaluating emerging gene-replacement therapies.

1.4.2 Advantages for Translational Studies

The scTSC2-KO model offers several key advantages for translational gene therapy research. First, the stochastic nature of TSC2 deletion utilized here generates focal pathological lesions surrounded by TSC2-competent cells. This allows direct assessment of both cell-autonomous and non-cell autonomous effects following AAV9 delivery of cTuberin (Cheah et al., 2021). Second, the postnatal onset of pathology creates a clinically realistic therapeutic window. Intervention can be administered around postnatal day 21, a little after seizure onset (around P9), which more closely reflects seizure onset and potential treatment timing in patients. This temporal window is not available in severe germline knockout models where pathology develops earlier and rapidly becomes lethal. Third, because Cre-mediated deletion in this model is largely restricted to CNS following neonatal ICV AAV1-Cre administration, therapeutic AAV9 delivery can be evaluated using systemic or intracranial routes. In this study, intracranial ICV administration was selected to directly assess CNS-targeted rescue while minimizing peripheral vector exposure. This strategy allows precise evaluation of brain-specific therapeutic efficacy in the context of stochastic TSC2 loss. Finally, the model supports robust, quantifiable translational endpoints, including survival, ventricular volume by

MRI, chronic ECoG quantification of seizures and high amplitude activities, cellular hypertrophy, pS6 levels, and behavioral performances (Cheah et al., 2021; Prabhakar et al., 2013). Together these features make the scTSC2-KO model an ideal platform for preclinical evaluation of AAV9-mediated condensed tuberin (cTuberin) replacement therapy.

1.5 Study Objectives and Hypothesis

1.5.1 Primary Aims

The primary aims of this study were:

1. To characterize the disease model by quantifying mTORC1 activity following TSC2 knockout in neurons.
2. To assess the impact of TSC2 loss on neuronal morphology.
3. To map the spatial distribution of TSC2 recombination across different brain regions.
4. To determine whether AAV9-mediated delivery of cTuberin helps reduce seizure frequency and duration.

Chapter 2: Materials and Methods

2.1 Stochastic, Cranial TSC2-KO Mouse Model

All experimental procedures were approved by the Institutional Animal Care and Use Committee for the Tufts University School of Medicine and Tufts Medical Center following the guidelines of the National Institutes of Health for the Care and Use of Laboratory Animals.

Animals were bred in-house and maintained under standard housing conditions with controlled temperature, a 12-hour light/dark cycle, and *ad libitum* access to food and water.

Experiments were performed using $TSC2^{fl/fl}$; $Ai9^{fl/fl}$ mice, which carry a Cre-inducible tdTomato reporter allele. To induce stochastic recombination in the developing brain, cryo-anesthetized neonatal pups (P0-P1) were injected with 1 μL of viral vector AAV1-CBA-Cre (2×10^{10} vg) into each lateral ventricle using a glass micropipette (70–100 μm in diameter at the tip; Figure 2.1A). Following injection, pups were placed on a warming pad and returned to their dam after observing full activity typical of newborn mice.

Cre-mediated recombination results in stochastic deletion of TSC2, producing a stochastic cranial TSC2 knockout (scTSC2-KO) model (Figure 2.1B). These mice exhibit spontaneous seizures and have a reduced lifespan due to seizure activity (Figure 2.1C). Control animals consisted of $TSC2^{fl/fl}$; $Ai9^{fl/fl}$ mice that did not receive postnatal AAV1-Cre injection.

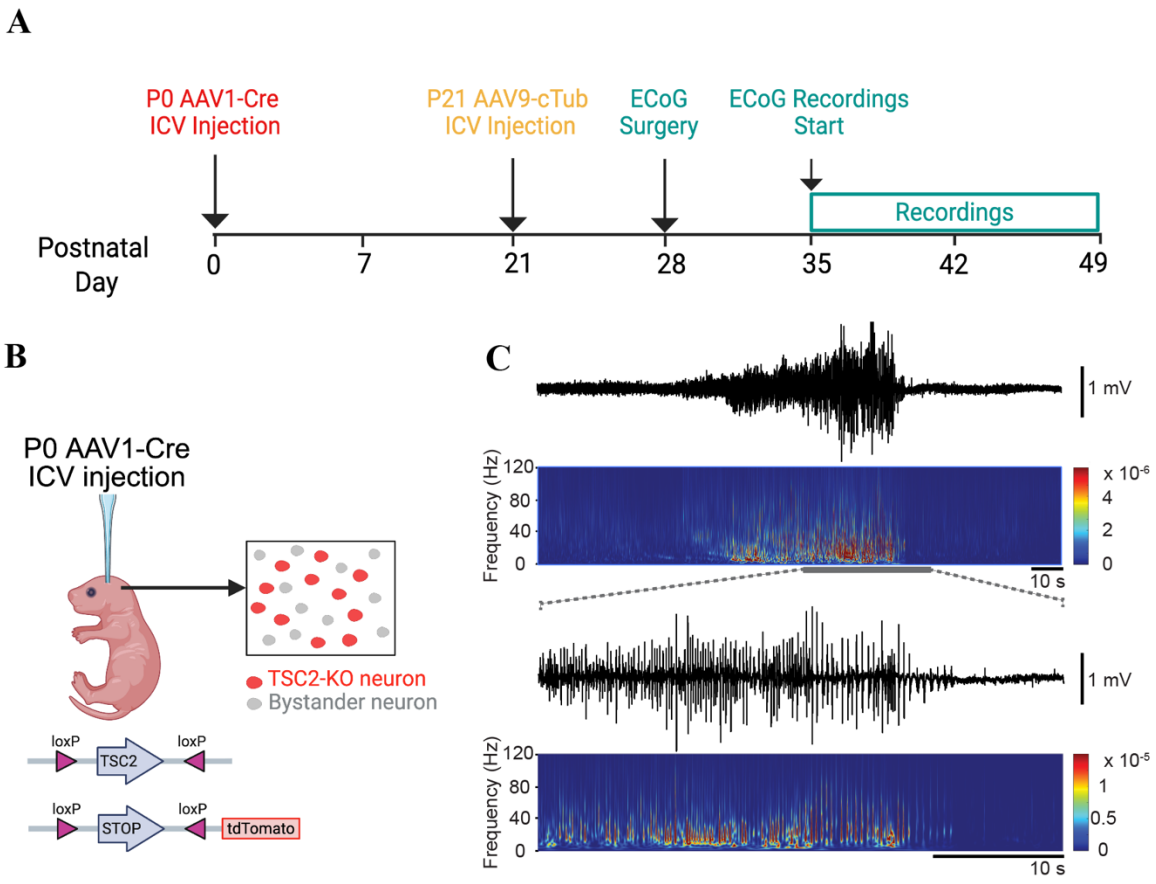

Figure 2.1 Experimental design and stochastic TSC2 knockout mouse model. (A) Experimental timeline illustrating the sequence of procedures. Neonatal mice received intracerebroventricular (ICV) injection of AAV1-Cre at P0 to induce stochastic deletion of TSC2 in the developing brain. At P21, animals received intracerebroventricular injection of AAV9-cTub or AAV9-EV. ECoG electrodes were implanted at P28, and electrophysiological recordings were performed for two weeks starting at P35. **(B)** Schematic of the stochastic cranial TSC2 knockout model. Neonatal intracerebroventricular injection of AAV1-Cre induces recombination in $TSC2^{fl/fl}$; $Ai9^{fl/fl}$ mice, resulting in a mosaic population of TSC2-deficient neurons (red) and bystander neurons (non-recombined: gray). Cre-mediated recombination also activates tdTomato reporter expression, enabling visualization of recombined cells. **(C)** Representative recorded spontaneous seizures from a scTSC2-KO mouse (top) and at an expanded timescale with Morlet wavelet scalograms for time-frequency information (bottom).

2.2 AAV Vector Design and Packaging

AAV vectors used in this study included AAV1-CBA-Cre, AAV9-EF1α-cTub-V5-GFP (AAV9-cTub; Figure 2.2A) and AAV9-EF1α-V5-GFP (AAV9-EV; Figure 2.2B). Viral particles were manufactured and obtained from Virovek (Houston, TX, USA).

The plasmid constructs pAAV9-EF1α-cTub-V5-GFP, and pAAV9-EF1α-V5-GFP were generated by our collaborators in the Breakefield Laboratory (Massachusetts General Hospital, Boston, MA, USA). The cTub construct encodes a condensed version of the Tuberin protein fused to a V5 epitope tag and GFP reporter under control of the EF1α promoter, enabling visualization and detection of transgene expression. The EV construct expresses V5-GFP alone and was used as a control in viral delivery experiments.

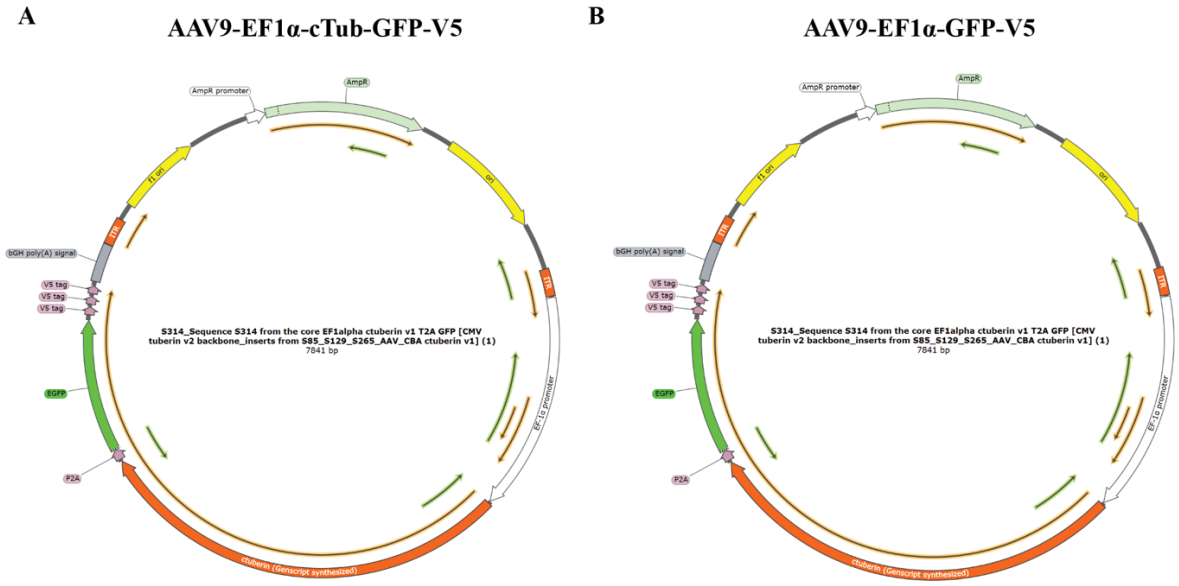

Figure 2.2 Schematic representation of AAV9 vectors used for gene delivery. (A) Map of the AAV9-EF1α-cTub-V5-GFP plasmid used to express the condensed Tuberin (cTub) therapeutic construct. The vector contains the EF1α promoter driving expression of the cTub transgene fused to a V5 epitope tag and GFP reporter, enabling detection of transgene expression by immunostaining and fluorescence imaging. **(B)** Map of the AAV9-EF1α-V5-GFP empty vector (EV) used as a control. This construct contains the EF1α promoter driving expression of V5-GFP without the cTub transgene, serving as a viral control for experiments evaluating the therapeutic effect of cTub expression. Both vectors contain the AAV inverted terminal repeats (ITRs) required for viral packaging and genome replication.

2.3 Immunohistochemistry

Mice were euthanized under isoflurane anesthesia at days 35-42 via transcardial perfusion with 1× PBS followed by 4% paraformaldehyde. Brains were fixed overnight at 4°C, cryoprotected in 30% sucrose for 24-48 hours, and embedded in optimal cutting temperature embedding medium (O.C.T) (Fisher Health Care), and 40 μm thick coronal sections were prepared. For immunohistochemistry, sections were blocked with 50% Bovine Serum Albumin (BSA) (Fisher bioreagents, lot# 251839, Massachusetts USA) and 100% goat serum (Sigma Aldrich, lot# SLBC7379V, St. Louis, Missouri USA) in 1× PBS containing 0.2% Triton X-100 for 1 h at room temperature (RT) and incubated overnight at 4°C with primary antibodies, including phospho-S6 (Ser 240-244, 1:800), anti-NeuN (1:500), GFP (1:1000). Details of primary antibodies dilutions and sources are provided (Table 2.3**)**. Following three washes with 1× PBS, sections were incubated with Alexa Fluor 488 (1:500), and Alexa Fluor 647 (1:500) for 2 hr at RT. Details of secondary antibodies dilutions and sources are provided (Table 2.3). Sections were washed three times with 1× PBS, with a final wash of 4',6-diamidino-2-phenylindole (Dapi) for 10 minutes (1:10,000). Slides were mounted on selectfrost microscope glass slides (fisherbrand, lot# 25305) using fluoromount-G (Invitrogen, lot#E143470).

Table 2.3 Antibodies

Primary Antibodies				
Antibody target	**Antibody species**	**Company**	**Lot #**	**Dilution to use**
NeuN	Mouse	EMD Millipore core	4031336	1:500
pS6 (Ser 240/244)	Rabbit	Cell signaling	18	1:800
GFP	Chicken	Abcam	Ab13970	1:1000
V5	Rabbit	Cell signaling	8	1:500

Secondary Antibodies				
Target Antibody	**Conjugate**	**Company**	**Lot#**	**Dilution to use**
Goat anti mouse	488	Jackson	545-146	1:500
Goat anti mouse	647	Jackson	115-605-062	1:500
Goat anti rabbit	647	Jackson	155622	1:500
Goat anti chicken	488	Abcam	AB6873	1:500

2.3.1 Image Acquisition

Fluorescent images were acquired using a Leica SP8 Falcon confocal microscope and a Leica DMi8 Thunder widefield fluorescence microscope (Leica Microsystems). For Thunder imaging, 10× and 20× air objectives were used to capture epifluorescence images. For confocal imaging on the SP8 Falcon, 20× oil and 40× oil immersion objectives were used.

Fluorophores included Dapi, GFP, pS6, NeuN, V5, and tdTomato expressed from Cre-dependent constructs. NeuN signals were detected using the Alexa Fluor 488 nm excitation laser (emission: 509-519 nm), while pS6 and V5 signals were detected using the Alexa Fluor 647 nm excitation laser (emission: 665-671 nm). tdTomato fluorescence from Cre expression was detected with excitation laser 561 nm (emission: 570-620 nm). Confocal images were acquired as z-stacks consisting of 10-11 optical sections (0.7 µm z-step size for representative images, and 1.0 µm for pS6 intensity and cell area analysis). Five optical sections from the z-stack were selected and maximum-intensity projected to generate a single image for analysis. In contrast, images acquired with the Thunder epifluorescence microscope were captured as single optical planes, for TSC2-KO distribution analysis. Under Thunder microscope exposure time for Dapi and tdTomato was at 50 s, NeuN was at 150 s, V5 and pS6 at 250 s.

Image acquisition was performed using Leica LAS X software (Leica Microsystems). For quantitative analysis, identical imaging parameters, including laser power, detector gain, and exposure settings, were maintained across all samples within each experiment.

2.3.2 Quantification of mTORC1 Activity

mTORC1 activity was assessed by measuring phosphorylated S6 (Ser 240/244) immunofluorescence intensity and cell morphology at both the single-cell and animal levels. Sections were co-stained with NeuN to identify neurons, Dapi to identify nuclei, and tdTomato expressed upon viral expression of Cre-recombinase that labels TSC2-KO cells.

For each mouse, three consecutive coronal sections (40 μm) containing the somatosensory cortex and hippocampus were selected for analysis. Images were acquired using falcon confocal images at 20× magnification, using identical acquisition settings across all experimental groups and quantification was done using ImageJ/fiji (version:1.54p, Bethesda, MD, USA).

Results are presented as both cell-level (Figure 3.1B, D) and mouse-level measurements. For mouse-level analysis, mean gray intensity and soma area values from all quantified neurons across the three sections were averaged to obtain a single mean value per animal for statistical analysis (Figure 3.1C, E). A total of four TSC2-KO mice and four wild-type controls were analyzed.

2.3.3 Quantification of TSC2-KO Neuron Distribution

Thunder fluorescence images were acquired at 10× magnification using a Leica THUNDER Imager epifluorescence microscope from three consecutive coronal sections containing the primary somatosensory cortex and hippocampus. Image analysis was performed using Fiji (ImageJ) with the ABBA (Atlas-Based Brain Analysis) extension

for atlas registration and QuPath for automated cell detection. Sections were registered to the Allen Mouse Brain Atlas to enable consistent delineation of anatomical boundaries and standardized selection of regions of interest (ROIs) across samples.

Automated cell detection was performed in QuPath using the StarDist deep-learning extension, which employs a convolutional neural network-based model to identify individual nuclei using star-convex polygon segmentation. For our purposes, StarDist was trained to detect NeuN positive neurons, across the brain regions including: retrosplenial cortex, motor cortex, somatosensory cortex, auditory cortex, CA1, CA3, dentate gyrus, thalamus, and caudate-putamen.

Initial cell detection training was performed using pS6 channel (Alexa 647 fluorophore as secondary) as the base channel because its signal provides clear visualization of neuronal soma size comparable to NeuN-positive neurons and tdTomato-positive TSC2-KO neurons. After successful base neuronal detection, the model was further trained using the NeuN channel and tdTomato channel to generate two separate classifiers: one identifying NeuN-positive neurons and one identifying tdTomato-positive neurons corresponding to TSC2-KO cells.

For final detection, multichannel images containing pS6, NeuN, and tdTomato signals were used to combine the trained classifiers to allow the model to detect and tease-apart NeuN-positive neurons and tdTomato-positive TSC2-KO neurons within the same multichannel image at once. After data collection, the proportion of TSC2-KO neurons in each region was calculated by normalizing the number of tdTomato-positive neurons to

the total number of NeuN-positive neurons within the same ROI, with results expressed as percentages.

2.4 AAV9 Gene Therapy Injection Protocol

In total 7 $TSC2^{fl/fl}Ai9^{fl/fl}$ mice that had received bilateral ICV AAV1-Cre at P0, received unilateral ICV treatment or control at P21. Mice were anesthetized with isoflurane (3% for induction in an induction chamber and maintained at 1.5–2% in oxygen at 0.5–1 L/min during the procedure). AAV9 vectors were administered via unilateral ICV injection using a microliter syringe (Hamilton company, Reno, NV, USA). Stereotaxic coordinates relative to bregma were: -0.2 mm anteroposterior (AP), 0.9 mm mediolateral (ML), 2.3 mm dorsolateral (DV). The injection needle was left in place for 5 minutes following infusion to minimize reflux before slow retraction.

AAV9-EF1α-cTuberin (AAV9-cTub) was injected at doses of 5×10^{11} vg/kg (2.13 µL per 10 g mouse). AAV9-EF1α-GFP empty vector (AAV9-EV) was administered at doses of 5×10^{11} vg/kg (2.19 µL per 10 g mouse, Virovek).

Intracerebroventricular delivery was selected to achieve controlled and CNS-restricted vector transduction in this initial therapeutic evaluation, allowing direct assessment of central rescue effects in the scTSC2-KO model.

In addition, as a control to assess successful vector delivery, 2 wild-type mice received 5×10^{13} vg/kg (double dose) of AAV9-cTub and AAV9-EV, to check for pure viral transfection of AAV9 construct.

2.5 ECoG Implant Surgery

In total, 7 $TSC2^{fl/fl}Ai9^{fl/fl}$ mice (28-30 weeks old, both sexes) that had received either high dose or low dose of AAV9-cTub or AAV9-EV were included in the study. Mice were anesthetized with isoflurane (3 vol% oxygen for induction, 1.5 vol% maintenance) and received pre-operative analgesia consisting of buprenorphine SR (0.5 mg/kg, subcutaneous; Wedgewood, Swedesboro, NJ, USA) and local analgesia with 0.25 % bupivacaine (2.5 mg/mL, subcutaneous) around the incision site. Animals were then secured in a stereotaxic frame, the dorsal skull was shaved and disinfected with iodine and 70% ethanol, and a midline scalp incision was made. The skull surface was cleaned, dried, and four burr holes (0.7 mm diameter; Item No. 19007-07, Fine Science Tools, Foster City, CA, USA) were drilled without penetrating the dura. Stereotaxic coordinates relative to bregma were as follows: anterior holes at AP -2.6 mm, ML ±2.0 mm (EEG and ground electrodes); posterior holes at AP -2.6 mm, ML ±2.5 mm (reference and ECoG electrodes). Four 0.1-inch stainless-steel screw electrodes with attached silver wires (Order # 8403, Pinnacle Technologies, Wyckoff, NJ, USA) were gently screwed into the burr holes and secured with dental cement and cyanoacrylate glue for increased implant stability allowing for multi-week ECoG recordings.

The silver wires were rapidly soldered to a four-channel head-mount (Order # 8402, Pinnacle Technologies, Wyckoff, NJ, USA) to minimize heat transfer, after which the entire implant was anchored to the skull with additional dental cement. Following surgery, mice were allowed to recover for at least 7 days before initiation of recordings and received supplemental buprenorphine (0.1 mg/kg, subcutaneous) as needed for post-operative pain.

2.5.1 ECoG Recordings

After recovering from surgery, a preamplifier (100 x gain, 1 Hz high-pass filter, Part # 8213, Pinnacle Technologies, Wyckoff, NJ, USA) was plugged into the implanted head-mount and preamplifiers were attached to a commutator in the ECoG recording system (Pinnacle Technologies, Wyckoff, NJ, USA). Mice were housed in a round, acrylic ECoG recording chamber with access to food and water *ad libitum* and kept on a standard light/dark cycle. Continuous 24-hr ECoG signals were acquired using a 100x gain preamplifier with 1Hz high-pass filter (Order#8213, Pinnacle Technologies, Wyckoff, NJ, USA) and simultaneously recorded (1kHz sampling rate) using custom script in LabChart Pro software (AD instruments, Colorado Springs, CO, USA) for at least 14 days. After recordings ended, ECoG signals were filtered (100 Hz low-pass filter) and recordings were manually reviewed by an experienced, blinded investigator. When seizures were identified, their duration was quantified, and their time of incidence was noted.

2.6 Statistics

All statistical analyses were performed using SigmaPlot for non-parametric and parametric tests, and R Studio for linear mixed-effects models (LMMs) utilizing the lme4 for lmer fits or nlme package. Data from *in vitro* and *in vivo* experiments were first assessed for normality using the Shapiro-Wilk test and for homogeneity of variances using Brown-Forsythe, Bartlett's, or Levene's tests (as appropriate for the distribution). Significance was set at $p = 0.05$ for all tests. P-values reported in the results section for omnibus tests (e.g., ANOVAs) refer to overall group or main effects, while those in figure legends indicate post-hoc pairwise comparisons (adjusted for multiple

comparisons). For independent group comparisons across more than two groups, the Kruskal-Wallis one-way ANOVA on ranks (1W ANOVA) was used, with Dunn's post-hoc test for pairwise comparisons.

For analyses of proportion of successful neuronal recombination across brain regions (e.g., regional tdTomato-positive cell/area quantification), where data were hierarchically structured (multiple regions sampled per animal, with potential animal-level variability), linear mixed-effects models (LMMs) were employed to account for repeated measures within animals and to estimate region-specific effects while controlling for random animal variation. LMMs were fit using restricted maximum likelihood (REML) estimation, with brain region as a fixed effect and animal as a random intercept. Percentage data were analyzed directly (or arcsin square root transformed if residuals deviated substantially from normality). Estimated marginal means (emmeans) were computed for each region, with Tukey-adjusted pairwise contrasts to evaluate key regional differences (e.g., retrosplenial cortex vs. other cortical/subcortical areas, hippocampal subfields CA1/CA3/DG, aggregated cortex vs. hippocampus vs. subcortical structures). This approach allowed robust handling of within-animal correlations and heterogeneous variances across regions. All p-values from post-hoc tests were adjusted for multiple comparisons (Tukey or equivalent), and trends ($0.05 < p < 0.10$) are noted where relevant for exploratory interpretation.

Lastly, the comparison between AAV9-cTub and AAV9-EV groups for seizure duration and frequency were performed using unpaired two-tailed Welch’s t-test (unequal variance assumed). Data are presented as mean ± standard deviation (SD) and standard error of mean (SEM). Statistical significance was defined as $p < 0.05$.

Chapter 3: Results

3.1 Validation of the Cranial Stochastic TSC2-KO Model

Clusters of tdTomato-positive neurons, indicating successful recombination and loss of TSC2 were observed in a subset of cells. Representative fluorescence images from the somatosensory cortex of a P35 scTSC2-KO that received AAV1-Cre injection show that distribution of tdTomato-positive cells was heterogeneous across the cortex, consistent with stochastic viral transduction (Figure 3.1A). To further confirm loss of TSC2-KO in cells marked with tdTomato, pS6 intensity and morphology in neurons were quantified.

3.1.1 Quantifying mTORC1 Activity

We expected that TSC2-KO would lead to cell-autonomous increase in mTORC1 signaling, that can be measured by quantifying downstream phosphorylated S6 (pS6; Ser240/244) immunofluorescence intensity. In addition, we monitored TSC2 wild-type (bystander) neurons from the same mouse/epileptic brain for potential non-cell-autonomous effects of TSC2-KO on bystander neurons.

At the single-cell level, pS6 intensity differed significantly between groups (1W ANOVA on ranks, $H(2) = 750.79$, $p < 0.001$). TSC2-KO neurons exhibited markedly elevated pS6 intensity compared with both bystander and wild-type neurons (Figure 3.1B). Median pS6 intensity values were 1640.45 a.u. (IQR: 1413.63 – 1916.16) for TSC2-KO neurons ($n = 457$ cells), 792.75 a.u. (IQR: 679.69 – 947.06) for bystander neurons ($n = 457$), and 964.59 a.u. (IQR: 807.02 – 1156.03) for wild-type neurons ($n = 480$ cells). Post-hoc Dunn's multiple comparison test confirmed that pS6 intensity in TSC2-KO neurons was significantly greater than both bystander and wild-type neurons ($p < 0.001$ for both

comparisons). Interestingly, bystander neurons exhibited slightly lower pS6 intensity than wild-type neurons, a difference that was also statistically significant ($p < 0.001$).

To account for clustering of cells within animals, analyses were repeated using animal-averaged values (n = 4 mice per cohort; Figure 3.1C). Mean pS6 intensity differed significantly between groups (1W ANOVA, $F(2,9) = 23.85$, $p < 0.001$). Mean pS6 intensity was 1680.60 ± 234.07 SD (SEM = ± 117.03) a.u. in TSC2-KO neurons, compared with 852.65 ± 122.15 SD (SEM = ± 61.08) a.u. in bystander neurons and 1001.83 ± 168.18 SD (SEM = ± 84.09) a.u. in wild-type neurons. Post-hoc Holm-Šidák comparisons confirmed significantly higher pS6 intensity in TSC2-KO neurons compared with both bystander and wild-type groups ($p < 0.001$), whereas bystander and wild-type neurons did not differ significantly ($p = 0.273$) at the mouse level. Together, these results demonstrate robust cell-autonomous activation of mTORC1 signaling in TSC2-deficient neurons.

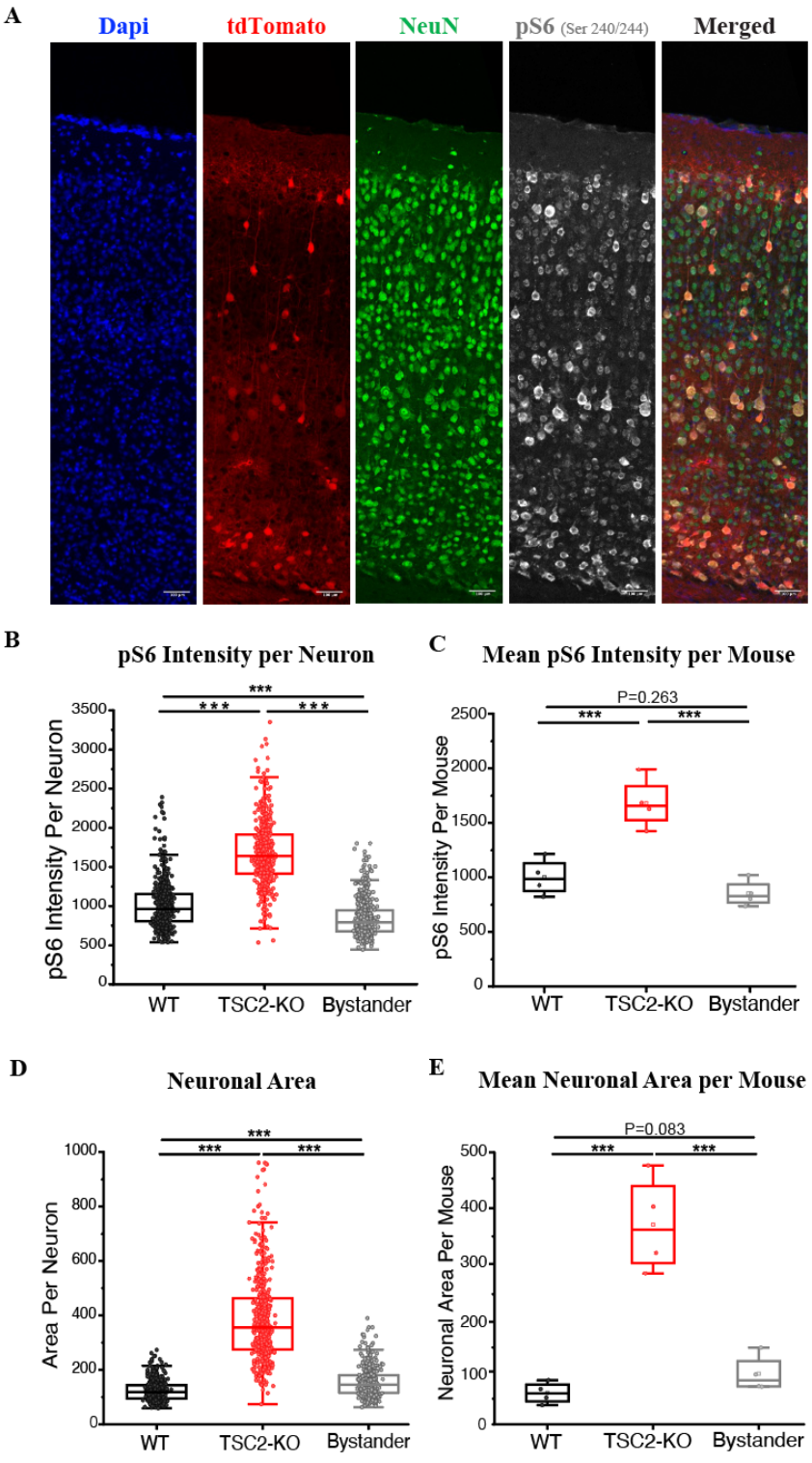

Figure 3.1 Stochastic TSC2 deletion increases mTORC1 signaling and neuronal soma size in the somatosensory cortex. (A) Representative images from layers I-VI of somatosensory cortex showing Dapi (nuclei), tdTomato (Cre-recombined/TSC2-KO cells), NeuN (neuronal marker), phosphorylated S6 (Ser240/244), and merged channels. Confocal 40 x magnification, scale bar = 100 µm. **(B)** Quantification of pS6 fluorescence intensity at the single neuron level. Each data point represents one neuron; boxes indicate median and interquartile range. pS6 intensity was significantly elevated in TSC2-KO neurons (n = 457) compared to WT (n = 480) and Bystander (n = 457) neurons. (1W-ANOVA on Ranks, Dunn's post hoc test, $p < 0.001$ for all pairwise comparisons). **(C)** When pS6 intensity was averaged per animal, we observed similar patterns with mean pS6 intensity being highest in TSC2-KO cells (average of 4 mice) than WT- (4 mice) and Bystander cells. (1W-ANOVA, Holm-Sidak post hoc, $p < 0.001$ for TSC2-KO vs. WT and Bystander, $p = 0.273$ for WT vs Bystander). **(D)** Quantification of neuronal soma area at the single-cell level. TSC2-KO mean soma area (n = 457) was significantly larger than WT (n = 480) and Bystander (n = 457) neurons (1W-ANOVA on Ranks, Dunn's post hoc test, $p < 0.001$ for all group comparisons). **(E)** Mean soma area of neurons averaged per animal. On the animal level, TSC2-KO neuronal soma size was significantly larger than WT- and Bystander somata (1W-ANOVA on Ranks, Student-Newman-Keuls post hoc test, $p = 0.009$ for TSC2-KO vs WT and Bystander, $p = 0.083$ for WT vs Bystander). For **(B) – (E)**: Shapiro-Wilk and Brown-Forsythe test were used to determine normal distribution and equal variance before testing for significant differences between cohorts.

3.1.2 Change in Neuronal Morphology

Since mTORC1 is associated with cell growth, we expected to see changes in neuronal morphology because of mTORC1 hyperactivation. At the single-cell level, neuronal soma area differed significantly between groups (1W ANOVA on ranks, $H(2) = 867.26$, $p < 0.001$; Figure 3.1D). Median soma area was 355.11 μm² (IQR: 274.57 – 464.75) in TSC2-KO neurons (n = 457 cells), compared with 145.55 μm² (IQR: 115.29 – 180.36) in bystander neurons (n = 457 cells) and 118.46 μm² (IQR: 94.64 – 143.2) in wild-type neurons (n = 480 cells). Dunn's post-hoc tests confirmed that TSC2-KO neurons were significantly larger than both bystander and wild-type neurons ($p < 0.001$ for both comparisons).

Animal-level analysis confirmed these findings. Neuronal soma area differed significantly between groups (1W ANOVA on ranks, $H(2) = 8.77$, $p = 0.012$; Figure 3.1D). Median soma area was 379.06 μm² (IQR: 318.81 – 463.46) in TSC2-KO neurons, compared with 143.71 μm² (IQR: 134.0 – 184.32) in bystander neurons and 123.28 μm² (IQR: 107.91 – 140.60) in wild-type neurons. Post-hoc comparisons indicated that TSC2-KO neurons were significantly larger than both bystander and wild-type neurons ($p = 0.009$), whereas no significant difference was observed between bystander and wild-type neurons ($p = 0.083$). These results demonstrate that postnatal TSC2 deletion induces pronounced neuronal hypertrophy in TSC2-deficient neurons, consistent with increased mTORC1 signaling.

3.2 Regional Distribution of TSC2-KO Neurons Between Cortex and Hippocampus

To examine regional differences in recombination, the proportion of tdTomato-positive (TSC2-KO) neurons was quantified in the cortex, including retrosplenial cortex (RSC), auditory cortex (AC), visual cortex, rhinal cortex, piriform cortex, somatosensory cortex (SSC), and temporal association area, as well as hippocampus, including CA1, CA2, CA3, the hilus, and the dentate gyrus (DG). The proportion of TSC2-KO neurons was calculated as the percentage of tdTomato-positive cells relative to the total number of NeuN-positive neurons within the cortex and hippocampus. When individual hemisphere measurements were analyzed (13 cortical hemispheres and 13 hippocampal hemispheres), the cortex exhibited a mean value of 3.16% ± 1.50 SD (SEM = ± 0.417), whereas the hippocampus showed a substantially higher mean of 35.95% ± 10.74 SD (SEM = ± 2.98; Figure 3.2B).

To account for the hierarchical structure of the data, including repeated measurements within animals and across slices; Linear mixed-effects models (LMM) was applied with sex, region (hippocampus and cortex), and left and right hemisphere as fixed effects and random intercepts for animal variation. Fixed effects were evaluated using Type III ANOVA. This analysis revealed a highly significant main effect of region ($F(1, 11.94) = 122.51$, $p = 1.24 \times 10^{-7}$), indicating the proportion of tdTomato-positive neurons was markedly higher in the hippocampus compared to the cortex (estimated difference = 32.80). In contrast, no significant effects of sex, or left versus right hemisphere were observed, suggesting that recombination levels were consistent across sexes and between hemispheres. Together these findings, indicate that regional identity, rather than sex or

hemispheric differences, is the primary determinant of recombination efficiency in this model.

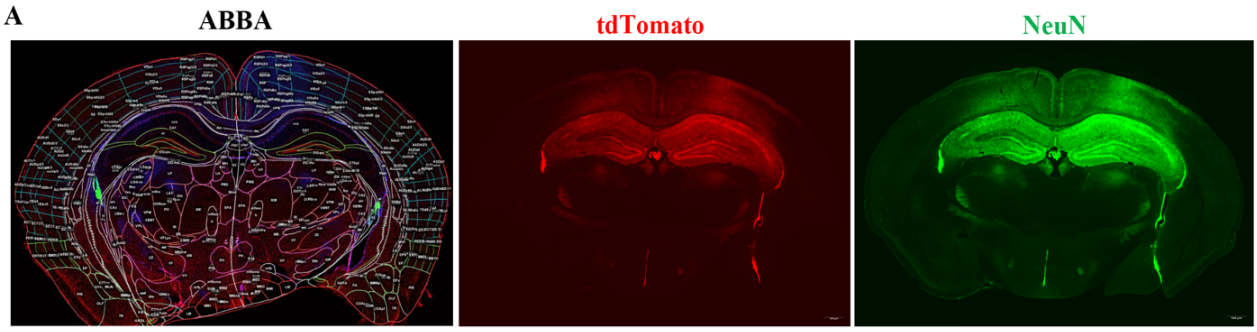

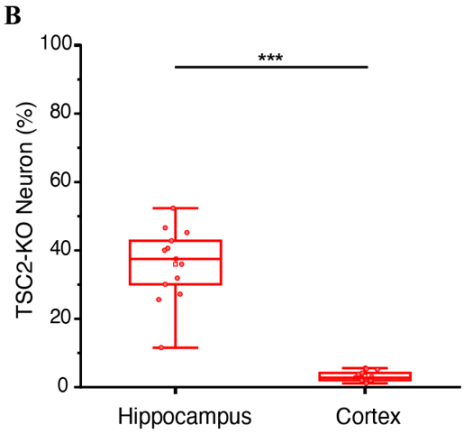

Figure 3.2 Distribution of TSC2-KO neurons in the somatosensory cortex and hippocampus. (A) Atlas-registered brain section (left) with annotated ROIs and representative epifluorescence image (20× magnification, scale bar = 500 μm) showing red TSC2-KO cells (center) and neurons identified by NeuN labeling (right). **(B)** Comparison of neuronal recombination rate in cortical regions (RSC, AC, visual, rhinal, piriform, and SSC, and temporal association area), as well as hippocampus (CA1, CA2, CA3, hilus and DG) show significantly higher rates of tdTomato-positive neurons in the hippocampus Mann-Whitney Rank Sum test, n = 13 hemisphere averages for hippocampus and cortex each, $p < 0.001$).

3.3 Distribution of TSC2-KO Neurons Across Smaller Brain Subregions

To further characterize the spatial heterogeneity of recombination, the percentage of TSC2-KO neurons was quantified across multiple cortical, hippocampal, and subcortical subregions. Due to the nested characteristic of the data, LMMs were used to account for repeated measurements within mice coming from multiple brain slices, and same regions, sex, and right and left hemispheres as fixed effects and mouse as random effect. Fixed effects were evaluated using Type III ANOVA.

Major brain divisions

When comparing the three major divisions (cortex, hippocampus, subcortex; n = 117 observations from 6 mice), TSC2-KO proportions differed dramatically (Type III ANOVA: $F(2, 109.8) \approx 31.5$, $p \approx 1.6 \times 10^{-11}$; Figure 3.3A). Highest TSC2-KO recombination rate was found to be in the hippocampus 19.88 ± 1.9% SE, intermediate in the cortex 6.04 ± 1.7% SE, and lowest in subcortical regions 0.55 ± 2.24% SE. Pairwise comparisons confirmed 13.85% higher proportions of TSC2-KO neurons in hippocampus than cortex ($p < 0.0001$) and 19.33% higher recombination rate than subcortex ($p < 0.0001$). In addition, cortex showed a marginally higher proportion of recombination than subcortex by 5.49% ($p \approx 0.079$). Inclusion of sex and hemisphere as covariates did not alter the strong effect of major brain division (p remained $\approx 10^{-11}$), and neither sex nor hemisphere contributed significantly.

Neocortex

Cortical subregions, including retrosplenial, motor, somatosensory, and auditory cortices, showed significant differences in the proportions of TSC2-KO neurons (n = 52 observations from 6 mice; Type III ANOVA: $F(3, 43.1) = 33.63$, $p = 2.3 \times 10^{-11}$; Figure 3.3B). TSC2-KO recombination rate was markedly higher in the retrosplenial cortex 17.8% ± 1.78 SE compared to other subregions: somatosensory cortex 3.74 ± 1.78% SE, motor cortex 6.10 ± 1.78% SE, and auditory cortex 1.93 ± 1.78% SE. All pairwise contrasts involving retrosplenial cortex were highly significant ($p < 0.0001$ vs. auditory, somatosensory, and motor). The motor cortex showed a marginally higher proportion of TSC2-KO neurons than auditory cortex ($p \approx 0.095$), while other pairwise differences

were non-significant. These results indicate strong subregion-specific enrichment of TSC2-KO neurons within cortex, primarily driven by the retrosplenial area.

Hippocampus

Analysis of hippocampal subregions, including CA1, CA3, and dentate gyrus (DG) (n = 39 observations from 6 mice) did not reveal significant patterns of variation (Type III ANOVA: $F(2, 31.8) = 2.32$, $p = 0.115$; Figure 3.3C). Proportion of TSC2-KO were approximately 14.6% in CA1, 15.2% in CA3, and 25.5% in the DG (SE = ± 4.97, for all). Pairwise comparisons showed no significant differences between any of the pairs. Thus, while the DG exhibited the highest average recombination rate, this trend did not reach statistical significance after correction.

Subcortical Regions

Subcortical structures, including thalamus and caudate-putamen, exhibited low recombination rates. TSC2-KO neuronal recombination was as low as 0.7% in the caudate-putamen and 0.6% in the thalamus, with no significant difference between regions (Tukey-adjusted $p > 0.05$; Figure 3.3D).

Overall, TSC2-KO neurons displayed pronounced spatial heterogeneity in this stochastic recombination model. The hippocampus, particularly the dentate gyrus, and the retrosplenial cortex emerged as the regions with the highest proportions, whereas subcortical areas showed almost negligible recombination, and most neocortical subregions remained low except the striking enrichment in retrosplenial cortex (Figure 3.4).

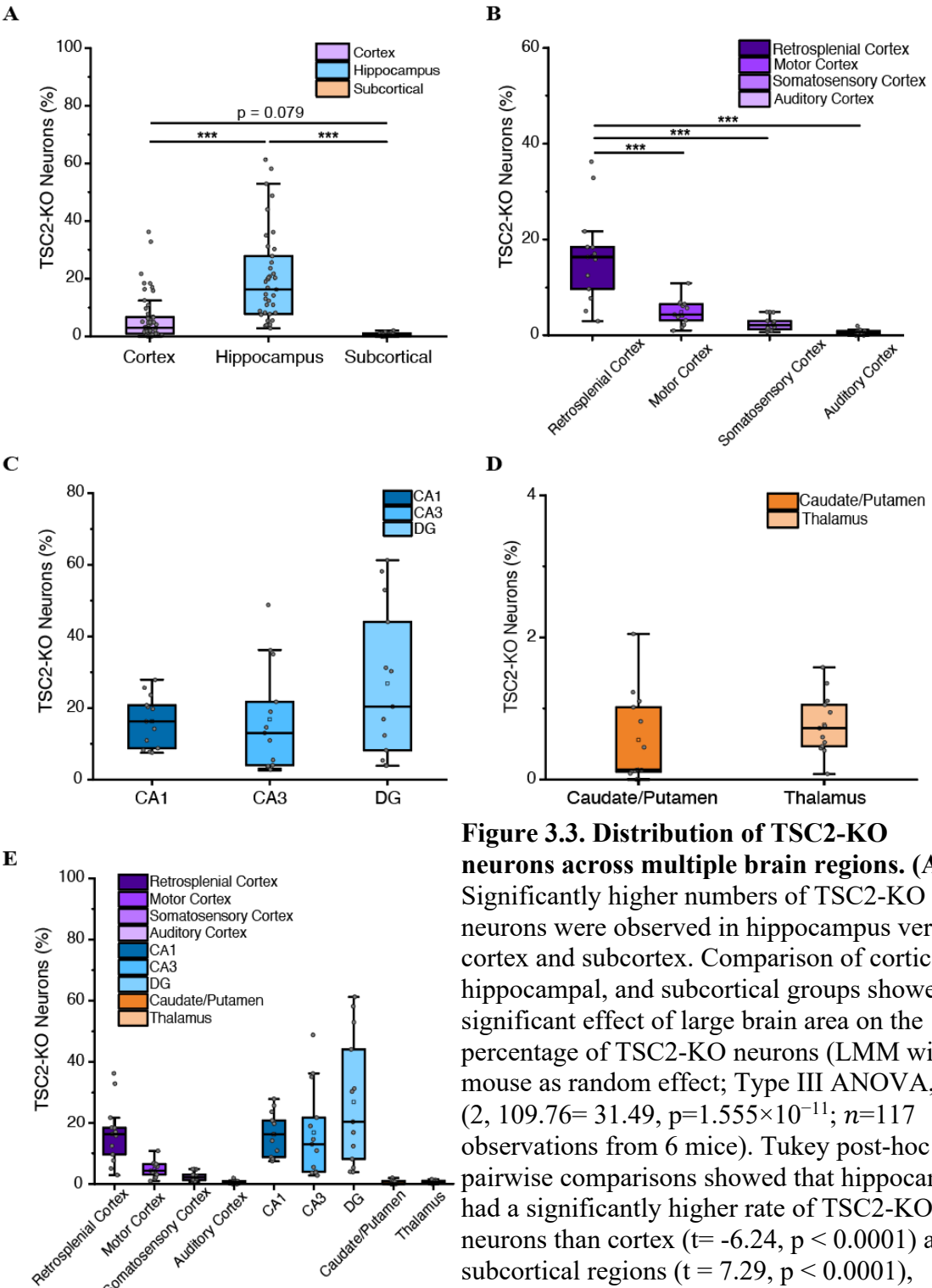

Figure 3.3. Distribution of TSC2-KO neurons across multiple brain regions. (A) Significantly higher numbers of TSC2-KO neurons were observed in hippocampus versus cortex and subcortex. Comparison of cortical, hippocampal, and subcortical groups showed a significant effect of large brain area on the percentage of TSC2-KO neurons (LMM with mouse as random effect; Type III ANOVA, F (2, 109.76= 31.49, p=1.555×10^{-11}; n=117 observations from 6 mice). Tukey post-hoc pairwise comparisons showed that hippocampus had a significantly higher rate of TSC2-KO neurons than cortex (t= -6.24, p < 0.0001) and subcortical regions (t = 7.29, p < 0.0001), whereas cortex and subcortical regions were not significantly different (t = 2.18, p= 0.079). **(B)** As in **(A)**, but for cortical subregions. Cortical subregions differed significantly in TSC2-KO rate (LMM with mouse as a random effect; Type III ANOVA, F (3, 43.07) = 33,63, p = 2.33×10^{-11}). Tukey post-hoc comparisons revealed

significantly higher rates of TSC2-KO neurons in RSC compared with AC (t= -9.11, P < 0.0001), MC (t = -6.72, p < 0.0001), and SSC (t = 8.07, p < 0.0001), and there was no significant difference between AC vs. SSC and (t = -1.036, p = 0.7295), and AC vs MC (t= -2.388, p = 0.0947). **(C)** As in **(A)**, but for hippocampal subregions. No significant effect of hippocampal subregion was detected (LMM with mouse as a random effect; Type III ANOVA, F (2, 31.79) = 2.32, p = 0.1145). Tukey post hoc comparisons showed no significant differences between CA1 and CA3 (t = -0.10, p = 0.9943), CA1 and DG (t = -1.92, p = 0.1510), or CA3 and DG (t = -1.81, p = 0.1815). **(D)** Distribution of TSC2-KO neurons in subcortical regions (caudate-putamen and thalamus). Both regions exhibited uniformly low recombination rates, with no significant difference between them (Tukey-adjusted p > 0.05). **(E)** Overview of regions that were statistically compared in (B) to (D). Percentage of tdTomato-positive (TSC2-KO) neurons was quantified across multiple cortical and subcortical regions, including retrosplenial cortex, motor cortex, somatosensory cortex, auditory cortex, entorhinal cortex, piriform cortex, hippocampal CA1, CA3, dentate gyrus (DG), caudate-putamen, thalamus, hypothalamus, globus pallidus, and amygdala. Counts were normalized to the total number of neurons within each region.

Note**:** Cortical and hippocampal quantification in this figure included slightly different subregions than in Figure 3.2. Cortical analysis here included retrosplenial, motor, somatosensory, and auditory cortices. Hippocampal quantification included DG, CA3, and CA1.

3.4. AAV9 Gene Therapy Study: *In vivo* ECoG Assessment of AAV9-Treated Mice

To determine whether AAV9-cTub delivery altered seizure activity in the scTSC2-KO model, chronic ECoG recordings were performed following viral administration (Figure 3.4A). Analysis of seizure activity focused on animals that received high-dose viral injections of both AAV9-cTub and AAV9-EV.

Electrographic recordings showed spontaneous seizures consistent with the expected seizure phenotype of the scTSC2-KO model (Figure 3.4B). These events were characterized by high-amplitude rhythmic discharges in the ECoG trace accompanied by increased power across multiple frequency bands in the spectrogram and followed by stereotypical post-ictal depression characteristic of generalized tonic-clonic seizures.

Analysis of seizure duration did not reveal a significant difference between treatment groups (Figure 3.4C). AAV9-cTub treated mice exhibited a mean duration of 42.13 ± 17.75 SD (SEM = 10.25, n = 3) seconds, whereas AAV9-EV treated mice exhibited a mean seizure duration of 31.86 ± 9.77 SD (SEM = 4.88, n = 4) seconds. This difference was also not significant (Welch's t-test: $t = 0.905$, $df = 2.91$, $p = 0.434$).

Similarly, seizure activity per hour showed that AAV9-cTub treated mice exhibited a mean seizure frequency of 0.292 ± 0.234 SD (SEM = 0.135, n = 3) and 0.12 ± 0.071 SD (SEM = 0.036, n = 4) in AAV9-EV treated mice (Figure 3.4D). This difference was not statistically significant (Welch's t-test: $t = 1.228$, $df = 2.28$, $p = 0.331$).

Thus, overall comparison between AAV9-cTub and EV-treated animals revealed no significant differences in seizure metrics. These findings indicate that AAV9-mediated delivery of condensed Tuberin did not produce a measurable improvement in electrographic seizure activity in the scTSC2-KO model under the condition tested.

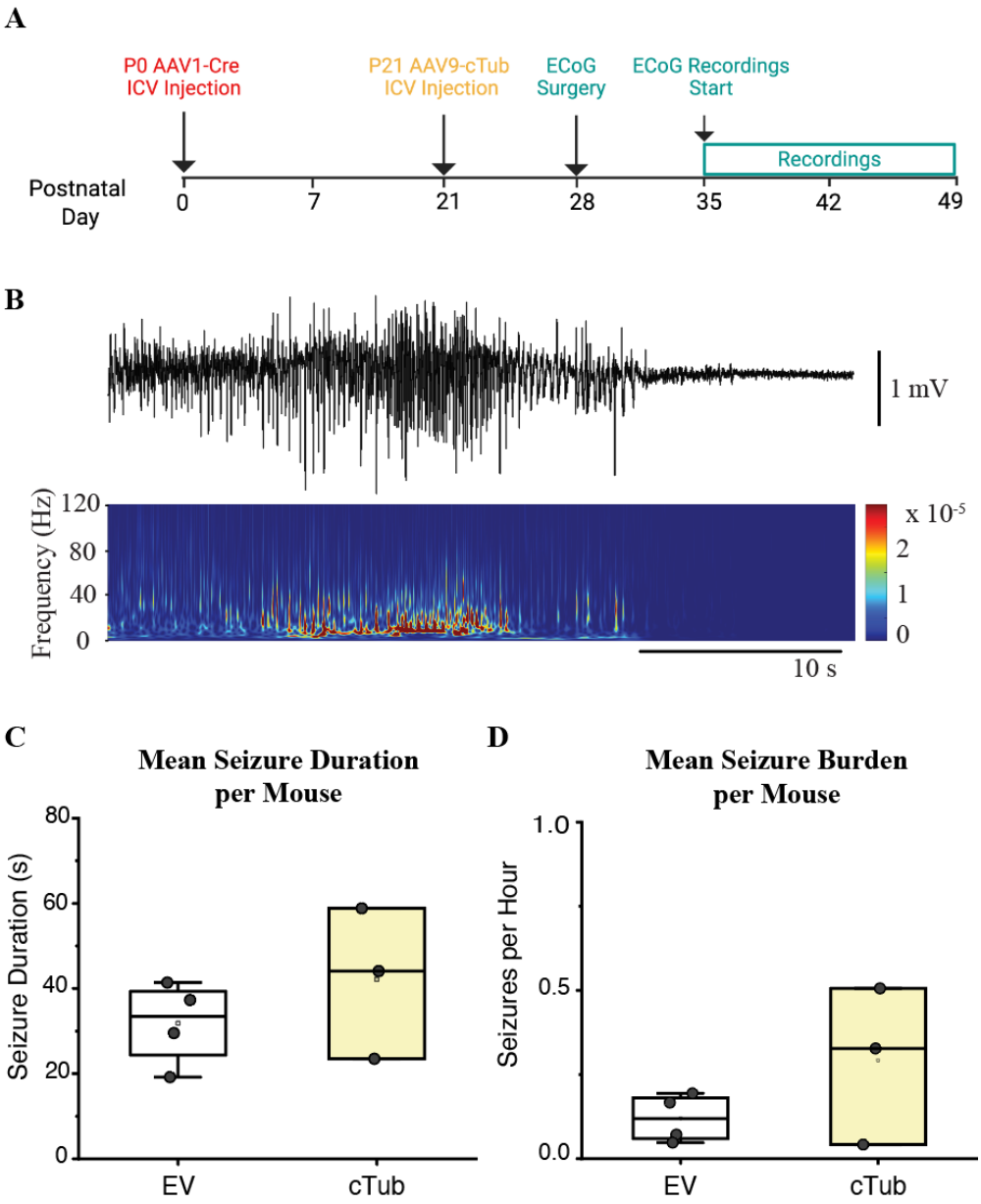

Figure 3.4. In vivo ECoG analysis of seizure activity following AAV9-mediated gene delivery in scTSC2-KO mice. (A) Experimental timeline illustrating AAV9-gene therapy injections and electrocorticogram recordings. Neonatal mice that had received ICV injection of AAV1-Cre at P0 to induce TSC2 deletion, at P21 received ICV injections of either AAV9-cTub or AAV9-EV. ECoG electrodes were implanted at P28, and recordings were collected for two weeks starting P35. **(B)** Representative ECoG trace showing spontaneous electrographic seizure activity in scTSC2-KO mice following AAV9-cTub injection. The lower panel shows the corresponding time–frequency spectrogram illustrating increased broadband power during seizure events. **(C)** Quantification of mean seizure duration per mouse. EV-treated mice exhibited a mean seizure duration of 31.9 s, whereas AAV9-cTub–treated mice exhibited a mean seizure duration of 42.1 s. No statistically significant differences were observed between treatment groups (Welch's t-test: $t = 0.905$, $p = 0.434$; AAV9-EV: $n = 4$ mice, AAV9-

cTub: n = 3 mice). **(D)** Quantification of mean seizure burden per mouse comparing EV and AAV9-cTub treated animals did not show significant anticonvulsant efficacy. Individual data points represent single animals. (Welch's t-test (equal variance not assumed): p = 0.331; AAV9-EV: n = 4 mice, AAV9-cTub: n = 3 mice).

3.5 Assessment of Viral Transgene Expression

Because no improvement in seizure phenotype was observed, we next examined AAV9-cTub and AAV9-EV expression in the brain. To investigate viral transduction efficacy, brain sections were analyzed using GFP immunostaining at 14 days and 28 days post-injection. Across all examined sections, GFP fluorescence remained undetectable (Figure 3.5A). To determine whether increasing viral dosage could improve expression, GFP expression from wild-type mice receiving double dose of AAV9-cTub or AAV9-EV substantially showed no detectable GFP.

The AAV construct included a triple V5 segment, and to further evaluate transgene expression, V5 immunostaining was performed to detect AAV9-cTub and AAV9-EV in the parenchyma. Only weak and sparse V5 signal was observed, primarily localized near lateral ventricles (Figure 3.5B) suggesting limited viral transduction and restricted expression of therapeutic construct.

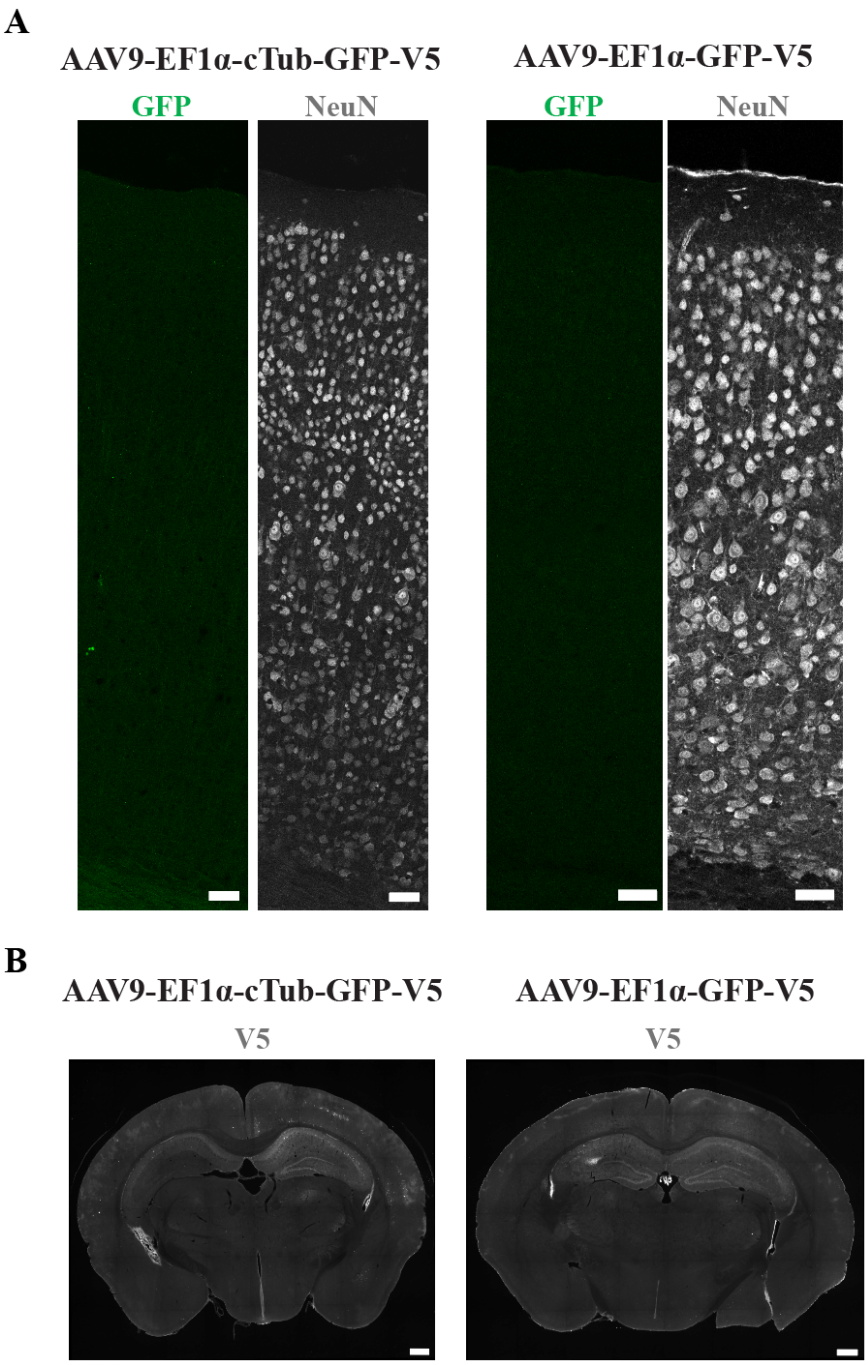

Figure 3.5. Assessment of AAV9-mediated transgene expression following viral delivery. (A) Representative images of cortical sections from mice injected with high-dose AAV9-cTub or AAV9-empty vector (EV), collected 14 days post-injection. GFP immunostaining was used to assess viral transduction efficiency, while NeuN staining marks neurons, GFP signal was largely undetectable across examined brain regions in both treatment groups, indicating minimal viral expression. Confocal microscope:40x magnification, scale bar = 100 µm. **(B)** Representative epifluorescence image from coronal brain sections showing V5 immunostaining used to detect expression of the V5-tagged cTub transgene. Only sparse and weak V5 signal was detected. Thunder microscope: 20x, scale bar = 500 µm. **Note:** Images shown are representative of 2 mice examined at 14 days post-injection of high dose AAV9-cTub and AAV9-EV.

3.5.1 Viral Genome Integrity

Sequencing analysis of packaged viral DNA showed that only ~8% of AAV9-cTub genomes contained the full-length functional cTuberin construct, compared with ~37% intact construct in the AAV9-empty vector preparation. These results indicate substantial truncation or incomplete packaging of the viral constructs, particularly in the AAV9-cTub preparation, consistent with the absent or extremely low level of GFP and V5 expression observed in these mice.

Chapter 4: Discussion

4.1 Molecular mTORC1 activity and Neuronal Morphology

In this study, we first validated the cranial scTSC2-KO mouse model by quantifying molecular and cellular consequences of TSC2 loss. Consistent with the established role of the TSC1/TSC2 complex as a negative regulator of mTORC1 signaling, neurons undergoing Cre-mediated recombination exhibited a robust increase in phosphorylated S6 (pS6), a canonical downstream marker of mTORC1 activity. Both single-cell and animal level analyses demonstrated significantly elevated pS6 intensity in the TSC2-deficient neurons compared with both wild-type and surrounding bystander neurons. These findings confirm that deletion of TSC2 produces strong cell- autonomous activation of mTORC1 signaling in this model.

To assess mTORC1 pathway activation, we quantified phosphorylation of ribosomal protein S6 at serine residues 240 and 244. These residues are phosphorylated downstream of S6 kinase, which is directly activated by mTORC1 signaling. As a result, phosphorylation at Ser240/244 is widely used as a reliable marker of mTORC1 pathway activity in both experimental models and human tissue (Figure 3.1A). Importantly, phosphorylation at these residues is considered more specific to mTORC1 signaling compared with other phosphorylation sites on S6 that may be influenced by additional kinases (i.e. Ser235/236). Therefore, the pS6 (Ser240/244) antibody was selected to specifically quantify mTORC1 activity within the scTSC2-KO model (Ruvinsky & Meyuhas, 2006; Biever et al., 2015). Consistent with our expectations, TSC2-KO neurons exhibited markedly increased pS6 intensity compared with wildtype and bystander neurons, which was accompanied by pronounced neuronal hypertrophy. These findings

align with the well-established role of mTORC1 as a central regulator of anabolic cellular processes. Persistent activation of this pathway following loss of TSC2 function is therefore expected to promote excessive neuronal growth and dysplastic morphology. Interestingly, analysis of non-recombined bystander neurons revealed a more complex pattern. At the single-cell level, bystander neurons exhibited slightly lower pS6 intensity compared with wild-type neurons (Figure 3.1B), whereas their soma size was modestly larger than that of wild-type neurons (Figure 3.1D). Although the reduction in pS6 intensity in bystander cells did not remain statistically significant when analyzed at the animal level (Figure 3.1C), the combination of reduced signaling with increased cell size presents an intriguing observation.

This discrepancy in statistical report from cell level to mouse level comparison likely reflects differences in statistical power between the two levels of analysis. At the single-cell level, the large number of observations provides high sensitivity to detect subtle differences, whereas the mouse-level analysis, with a relatively small cohort size (TSC2-KO = 4 mice, WT= 4 mice), is underpowered and therefore less capable of detecting small effect sizes. While such a sample size is sufficient to identify large, robust effects (e.g., near complete seizure reduction), it is unlikely to reliably capture modest differences (<20%) between groups. In terms of the difference seen in bystander neurons in the pS6 intensity data and soma area compared to WT, one possible explanation could be that mosaic deletion of TSC2 may produce non-cell-autonomous effects within the surrounding neural microenvironment. Hypertrophic TSC2-deficient neurons may alter local synaptic activity, metabolic demands, or extracellular signaling, thereby influencing surrounding wild-type neurons. Changes in network activity or altered excitatory-

inhibitory balance could potentially drive structural plasticity in bystander neurons even in the absence of direct mTORC1 hyperactivation. Alternatively, increased soma size in bystander neurons could reflect compensatory structural responses to altered network dynamics generated by nearby large TSC2-deficient neurons in the network connection. Because the scTSC2-KO model produces a heterogeneous distribution of mutant cells embedded within largely normal tissue, it provides a unique opportunity to examine both cell-autonomous and non-cell autonomous consequences of TSC2 loss. Further investigation will be required to determine whether these subtle morphological changes in bystander neurons reflect compensatory mechanisms, altered synaptic input, or early stages of network remodeling associated with epileptogenesis.

Overall, these results validate the scTSC2-KO model as a robust system for studying the cellular consequences of TSC2 loss. The presence of strong mTORC1 activation and neuronal hypertrophy in recombined neurons confirms that this model produces key molecular and cellular features of TSC neuropathology, providing a reliable platform for evaluating therapeutic strategies aimed at restoring TSC complex function.

4.2 Distribution of TSC2-KO Neurons

An additional objective of this study was to characterize the spatial distribution of Cre-mediated recombination in the scTSC2-KO model. Understanding the pattern of TSC2 deletion is important because the location and density of mutant neurons may influence the emergence and propagation of epileptiform activity. Initial comparison between the cortex, including RSC, AC, visual, rhinal, piriform, and SSC, and temporal association area, as well as hippocampus, including CA1, CA2, CA3, hilus and DG revealed a

striking regional difference in recombination rates (Figure 3.2B). The proportion of TSC2-KO neurons was significantly higher in hippocampus than in the cortex. This finding suggests that the efficiency of AAV1-Cre-mediated recombination varies substantially across brain regions following neonatal ICV injection. Because the hippocampus and RSC are adjacent to the lateral ventricles, it is likely exposed to higher local concentrations of viral particles immediately following injection, which may contribute to the elevated recombination rate observed in these regions close to the ventricles.

Given the large differences observed between the two regions, we performed more detailed analysis by subdividing coronal brain sections into multiple anatomical subregions including, cortical (only RSC, MC, SSC, and AC), hippocampal (only CA1, CA3, DG), and subcortical structures (Figure 3.3A). Within the neocortex, the RSC stood out with highest proportion of TSC2-KO neurons, whereas areas such as SSC, MC, and AC showed substantially lower recombination rates (Figure 3.3B). Importantly, TSC2-KO neurons were most abundant in hippocampus across CA1, CA3, and DG subfields, with the dentate gyrus showing a slightly higher proportion (Figure 3.3C). These regional differences likely arise from variations in viral diffusion, proximity to ventricular space, local cytoarchitecture, neuronal connectivity patterns, and developmental timing, all of which can influence AAV1-Cre transduction efficiency across brain structures. No difference between sexes and left versus right hemispheres were observed.

Taken together, these results demonstrate that Cre-mediated recombination in the scTSC2-KO model is region-dependent, with hippocampus showing the greatest susceptibility to recombination and subcortical regions remaining largely unaffected. This

uneven distribution of TSC2-KO deficient neurons has important implications for the interpretation of network-level phenotypes in this model. Because the hippocampus is strongly implicated in seizure generation, propagation, and generalization, the elevated density of TSC2-KO neurons in this region may contribute to the spontaneous seizures in this model.

More broadly, these findings highlight an important feature of stochastic gene deletion models: the spatial pattern of recombination can strongly influence disease phenotypes. Mapping the regional distribution of mutant neurons therefore provides critical context for interpreting both cellular and network-level consequences of TSC2 loss and for evaluating the efficacy of therapeutic interventions targeting these pathological circuits.

4.3 Gene Therapy Study

To evaluate the functional effects of AAV9-mediated cTuberin delivery, we performed chronic ECoG recordings following viral administration. Treated animals continued to exhibit spontaneous electrographic seizures that were comparable to those observed in mice receiving the empty vector control. Quantitative analysis of seizure frequency and duration revealed no detectable improvement in seizure phenotype following AAV9-cTub treatment (Figure 3.4).

Because the absence of therapeutic effect could reflect failure of viral transduction, we next examined transgene expression in treated animals. However, GFP immunostaining revealed no detectable GFP signal in brain sections collected 14 and 28 days following viral injection in scTSC2-KO mice (Figure 3.5). In addition, wild type mice injected with

double dose of AAV9-cTub or AAV9-EV were also examined 20 days post injection, GFP staining was similarly absent in these animals.

Immunostaining for the V5 epitope tag, present in both constructs, showed only weak focal expression in the subventricular zone, suggesting extremely limited expression of the viral construct. To investigate the underlying cause of this limited expression, we sequenced the packaged constructs. Sequencing of packaged viral genomes further demonstrated only a small portion of vectors contained the full-length functional construct for both AAV9-cTub (~8%) and AAV9-EV (~37%). Studies analyzing capsid composition have shown that only capsids containing intact genomes produce functional transgene expression, whereas partially packaged or truncated genomes contribute to vector titer but do not generate therapeutic protein (McColl-Carboni et al., 2024). In addition, purified therapeutic AAV preparations generally contain a much higher proportion of genome-containing particles, often exceeding 70-80%, highlighting the importance of vector genome integrity for achieving adequate transgene expression (Khaparde et al., 2025).

Another potential explanation for the absence of detectable GFP signal relates to known limitations of GFP reporter systems. GFP-based reporters require relatively high levels of protein expression to generate detectable fluorescence *in vivo* because each GFP molecule produces only a single fluorophore and the system lacks signal amplification. As a result, weak or transient transgene expression can fall below the detection threshold even when viral genomes are present in target cells (Serganova et al., 2019). To address this possibility experimentally, we first performed acute imaging of GFP fluorescence in tissue slices and subsequently used GFP immunostaining followed by imaging to enhance

detection sensitivity. However, neither approach revealed clear GFP-positive cells, suggesting that the lack of signal was not simply due to limitations of direct fluorescence imaging alone (Figure 3.5A).

In our vector, GFP was positioned immediately downstream of cTuberin and linked by a P2A sequence, and the triple V5 epitope tag was located further downstream, after GFP, and was included to facilitate detection of expressed protein. Therefore, the absence of detectable GFP signal is more likely to reflect low overall expression, incomplete or inefficient packaging of viral genome, or instability affecting the integrity of the construct. Yet, the weak V5 signal observed in some cells suggests that a small fraction of viral genomes retained sufficient integrity to permit minimal transgene expression (Figure 3.5B).

Taken together, these findings suggest that the lack of therapeutic efficacy observed in the present study is likely attributable to inefficient packaging and reduced functional genome content in the viral preparation rather than a failure of the gene replacement strategy itself.

4.4 Limitations

Several limitations should be considered when interpreting the results of the AAV9-mediated gene therapy study. The most significant limitation relates to the integrity of the viral construct used for gene delivery. Because only capsids containing full-length genomes are capable of producing functional transgene expression, the low proportion of intact construct resulted in a substantial reduction in the number of cells receiving a functional therapeutic construct.

A second limitation relates to the size of the cTuberin construct relative to the packaging capacity of AAV vectors. The maximal packaging capacity of AAV is approximately 4.7-5.0 kb, and the cTub construct with additional GFP and triple V5 is approaching this limit and is prone to incomplete packaging and truncated genomes in the AAV packaging process.

Another limitation involves the distribution of viral transduction following ICV injection. Although ICV delivery can achieve widespread central nervous system exposure, viral distribution may vary across brain regions and may not uniformly target neuronal populations that are most relevant for seizure generation. In the scTSC2-KO model used in this study, recombination was particularly enriched in hippocampal regions, suggesting that efficient therapeutic targeting of these circuits may be critical for modifying seizure phenotypes. Limited AAV9-cTub expression in these regions could therefore reduce the likelihood of detecting a therapeutic effect. This heterogeneity can be exacerbated by alterations in CSF flow in hydrocephalic craniums of TSC2-KO mice. Targeting of ventricular spaces for injection purposes is not trivial given the growth and resulting anatomical aberrations of the ventricular spaces.

Finally, the relatively small number of animals included in electrophysiological analyses may limit the statistical power to detect subtle treatment effects. Although spontaneous seizures were reliably detected in both treatment groups, larger cohorts would improve the ability to detect moderate changes in seizure burden.

4.5 Future Directions

Future studies should focus on improving the efficiency and integrity of the viral vector used for TSC2 gene replacement. Optimization of viral genome packaging will be critical for increasing the proportion of functional cTub construct and ensuring robust transgene expression *in vivo*. This may include refining the vector design to better accommodate the size constraints of AAV vectors for example by excluding the GFP cassette, and optimizing plasmid production methods, or implementing improved purification strategies to enrich for capsids containing full-length genomes.

Future experiments should also further characterize the spatial distribution of AAV9-cTub transduction following delivery and check its impact as a therapeutic agent, first at the network level for seizure frequency and duration, second at the cellular level for potential impact on the intrinsic excitability of TSC2-KO neurons and, third at the molecular level to check for potential reduction in mTORC1 hyperactivation by looking at the phosphorylation levels of S6 protein (Ser240/244). In terms of the health and quality of the delivery, cTuberin should be monitored from the process of transcription (mRNA levels, and functionality) to translation (cTub expression and its binding to the hamartin counterpart).

In addition, because the hippocampus exhibited the highest rate of TSC2 recombination in this model, targeting this region effectively may be particularly important for modifying seizure phenotypes. Alternative delivery routes or optimized capsids with improved neuronal tropism and BBB penetration may help increase transduction efficiency in key epileptogenic circuits.

Additional work is necessary to determine whether successful restoration of TSC complex function through gene replacement can normalize mTOR signaling and reduce seizure activity in this model *in vivo*. Once vector design and packaging efficiency are improved, future studies will evaluate whether robust cTuberin expression can reverse the cellular and network-level abnormalities associated with TSC2 loss.

References

Abou Haidar, E., Prabhakar, S., Geffrey, A. L., Mahamdeh, M., Tomeh, T., Breyne, K., Roumieh, E., Gurevich, M., Soberman, R. J., Wojtkiewicz, G. R., Chen, J. W., Han, J. S., Stemmer-Rachamimov, A., & Breakefield, X. O. (2025). AAV hamartin gene therapy in a stochastic, cerebral mouse model of tuberous sclerosis type 1. *Mol Ther Methods Clin Dev*, *33*(3), 101556. https://doi.org/10.1016/j.omtm.2025.101556

Bankhead, P. et al. QuPath: Open source software for digital pathology image analysis. *Scientific Reports* (2017). https://doi.org/10.1038/s41598-017-17204-5

Bateup, H. S., Johnson, C. A., Denefrio, C. L., Saulnier, J. L., Kornacker, K., & Sabatini, B. L. (2013). Excitatory/inhibitory synaptic imbalance leads to hippocampal hyperexcitability in mouse models of tuberous sclerosis. *Neuron*, *78*(3), 510–522. https://doi.org/10.1016/j.neuron.2013.03.017

Bennett, A., Mietzsch, M., & Agbandje-McKenna, M. (2017). Understanding capsid assembly and genome packaging for adeno-associated viruses. *Future Virol*, *12*(6), 283–297. https://doi.org/10.2217/fvl-2017-0011

Caban, C., Khan, N., Hasbani, D. M., & Crino, P. B. (2017). Genetics of tuberous sclerosis complex: implications for clinical practice. *Appl Clin Genet*, *10*, 1–8. https://doi.org/10.2147/tacg.S90262

Chan, K. Y., Jang, M. J., Yoo, B. B., Greenbaum, A., Ravi, N., Wu, W. L., Sánchez-Guardado, L., Lois, C., Mazmanian, S. K., Deverman, B. E., & Gradinaru, V. (2017). Engineered AAVs for efficient noninvasive gene delivery to the central and peripheral nervous systems. *Nat Neurosci*, *20*(8), 1172–1179. https://doi.org/10.1038/nn.4593

Cheah, P. S., Prabhakar, S., Yellen, D., Beauchamp, R. L., Zhang, X., Kasamatsu, S., Bronson, R. T., Thiele, E. A., Kwiatkowski, D. J., Stemmer-Rachamimov, A., György, B., Ling, K. H., Kaneki, M., Tannous, B. A., Ramesh, V., Maguire, C. A., & Breakefield, X. O. (2021). Gene therapy for tuberous sclerosis complex type 2 in a mouse model by delivery of AAV9 encoding a condensed form of tuberin. *Sci Adv*, *7*(2). https://doi.org/10.1126/sciadv.abb1703

Chen, C. S., & Aylett, C. H. S. (2025). New insights into tuberous sclerosis complex: from structure to pathogenesis. *Front Cell Dev Biol*, *13*, 1595867. https://doi.org/10.3389/fcell.2025.1595867

Chong-Kopera, H., Inoki, K., Li, Y., Zhu, T., Garcia-Gonzalo, F. R., Rosa, J. L., & Guan, K. L. (2006). TSC1 stabilizes TSC2 by inhibiting the interaction between TSC2 and the HERC1 ubiquitin ligase. *J Biol Chem*, *281*(13), 8313–8316. https://doi.org/10.1074/jbc.C500451200

Chu-Shore, C. J., Major, P., Camposano, S., Muzykewicz, D., & Thiele, E. A. (2010). The natural history of epilepsy in tuberous sclerosis complex. *Epilepsia*, *51*(7), 1236–1241. https://doi.org/10.1111/j.1528-1167.2009.02474.x

Conte, E., Boccanegra, B., Dinoi, G., Pusch, M., De Luca, A., Liantonio, A., & Imbrici, P. (2024). Therapeutic Approaches to Tuberous Sclerosis Complex: From Available Therapies to Promising Drug Targets. *Biomolecules*, *14*(9). https://doi.org/10.3390/biom14091190

Created in BioRender. abdollahpour, N. (2026) https://BioRender.com/s1xhn8p

Cusmai, R., Moavero, R., Bombardieri, R., Vigevano, F., & Curatolo, P. (2011). Long-term neurological outcome in children with early-onset epilepsy associated with tuberous sclerosis. *Epilepsy Behav*, *22*(4), 735–739. https://doi.org/10.1016/j.yebeh.2011.08.037

Dabora, S. L., Jozwiak, S., Franz, D. N., Roberts, P. S., Nieto, A., Chung, J., Choy, Y. S., Reeve, M. P., Thiele, E., Egelhoff, J. C., Kasprzyk-Obara, J., Domanska-Pakiela, D., & Kwiatkowski, D. J. (2001). Mutational analysis in a cohort of 224 tuberous sclerosis patients indicates increased severity of TSC2, compared with TSC1, disease in multiple organs. *Am J Hum Genet*, *68*(1), 64–80. https://doi.org/10.1086/316951

Davis, P. E., Filip-Dhima, R., Sideridis, G., Peters, J. M., Au, K. S., Northrup, H., Bebin, E. M., Wu, J. Y., Krueger, D., & Sahin, M. (2017). Presentation and Diagnosis of Tuberous Sclerosis Complex in Infants. *Pediatrics*, *140*(6). https://doi.org/10.1542/peds.2016-4040

Detrait, E. R., Bowers, W. J., Halterman, M. W., Giuliano, R. E., Bennice, L., Federoff, H. J., & Richfield, E. K. (2002). Reporter gene transfer induces apoptosis in primary cortical neurons. *Mol Ther*, *5*(6), 723–730. https://doi.org/10.1006/mthe.2002.0609

Deverman, B. E., Pravdo, P. L., Simpson, B. P., Kumar, S. R., Chan, K. Y., Banerjee, A., Wu, W. L., Yang, B., Huber, N., Pasca, S. P., & Gradinaru, V. (2016). Cre-dependent selection yields AAV variants for widespread gene transfer to the adult brain. *Nat Biotechnol*, *34*(2), 204–209. https://doi.org/10.1038/nbt.3440

Dufner-Almeida, L. G., Cardozo, L. F. M., Schwind, M. R., Carvalho, D., Almeida, J. P. G., Cappellano, A. M., Alegria, T. G. P., Nanhoe, S., Nellist, M., Passos-Bueno, M. R., Chiavegatto, S., Silva, N. S., Rosemberg, S., Pereira, A. P. A., Antoniuk, S. A., & Haddad, L. A. (2024). Molecular and Functional Assessment of TSC1 and TSC2 in Individuals with Tuberous Sclerosis Complex. *Genes (Basel)*, *15*(11). https://doi.org/10.3390/genes15111432

Ercan, E., Han, J. M., Di Nardo, A., Winden, K., Han, M. J., Hoyo, L., Saffari, A., Leask, A., Geschwind, D. H., & Sahin, M. (2017). Neuronal CTGF/CCN2 negatively regulates myelination in a mouse model of tuberous sclerosis complex. *J Exp Med*, *214*(3), 681–697. https://doi.org/10.1084/jem.20160446

Foust, K. D., Nurre, E., Montgomery, C. L., Hernandez, A., Chan, C. M., & Kaspar, B. K. (2009). Intravascular AAV9 preferentially targets neonatal neurons and adult astrocytes. *Nat Biotechnol*, *27*(1), 59–65. https://doi.org/10.1038/nbt.1515

French, J. A., Lawson, J. A., Yapici, Z., Ikeda, H., Polster, T., Nabbout, R., Curatolo, P., de Vries, P. J., Dlugos, D. J., Berkowitz, N., Voi, M., Peyrard, S., Pelov, D., & Franz, D. N. (2016). Adjunctive everolimus therapy for treatment-resistant focal-onset seizures associated with tuberous sclerosis (EXIST-3): a phase 3, randomised, double-blind, placebo-controlled study. *Lancet*, *388*(10056), 2153–2163. https://doi.org/10.1016/s0140-6736(16)31419-2

Furber, A., Martin, A., Bertuzzi, A., Wesson, F., Harrison, M., Bowditch, S., & Siddiqui, J. (2025). Burden of illness in tuberous sclerosis complex-associated epilepsy: a systematic literature review of epidemiology, health-related quality of life, costs and resource use. *Orphanet J Rare Dis*, *20*(1), 609. https://doi.org/10.1186/s13023-025-03975-y

Giannikou, K., Lasseter, K. D., Grevelink, J. M., Tyburczy, M. E., Dies, K. A., Zhu, Z., Hamieh, L., Wollison, B. M., Thorner, A. R., Ruoss, S. J., Thiele, E. A., Sahin, M., & Kwiatkowski, D. J. (2019). Low-level mosaicism in tuberous sclerosis complex: prevalence, clinical features, and risk of disease transmission. *Genet Med*, *21*(11), 2639–2643. https://doi.org/10.1038/s41436-019-0562-6

Guo, D., Zhang, B., Han, L., Rensing, N. R., & Wong, M. (2024). Cerebral vascular and blood brain-barrier abnormalities in a mouse model of epilepsy and tuberous sclerosis complex. *Epilepsia*, *65*(2), 483–496. https://doi.org/10.1111/epi.17848

Hale, A. T., Savage, C., Estevez-Ordonez, D., Oliver, T., Hedaya, A., Wang, S., Ragheb, J., Vignoli, A., Carlson, C., Liu, T., Yuan, L., Wang, Y., Chivukula, S., Fallah, A., Mohamed, I., Bebin, E. M., Rozzelle, C. J., Weiner, H. L., Liang, S., & Blount, J. P. (2025). Epilepsy surgery outcomes in children with tuberous sclerosis complex: a systematic review and meta-analysis. *J Neurosurg Pediatr*, *35*(6), 599–611. https://doi.org/10.3171/2024.12.Peds24311

Hinderer, C., Katz, N., Buza, E. L., Dyer, C., Goode, T., Bell, P., Richman, L. K., & Wilson, J. M. (2018). Severe Toxicity in Nonhuman Primates and Piglets Following High-Dose Intravenous Administration of an Adeno-Associated Virus Vector Expressing Human SMN. *Hum Gene Ther*, *29*(3), 285–298. https://doi.org/10.1089/hum.2018.015

Huang, J., Dibble, C. C., Matsuzaki, M., & Manning, B. D. (2008). The TSC1-TSC2 complex is required for proper activation of mTOR complex 2. *Mol Cell Biol*, *28*(12), 4104–4115. https://doi.org/10.1128/mcb.00289-08

Jansen, F. E., Vincken, K. L., Algra, A., Anbeek, P., Braams, O., Nellist, M., Zonnenberg, B. A., Jennekens-Schinkel, A., van den Ouweland, A., Halley, D., van Huffelen, A. C., & van Nieuwenhuizen, O. (2008). Cognitive impairment in tuberous sclerosis complex is a multifactorial condition. *Neurology*, *70*(12), 916–923. https://doi.org/10.1212/01.wnl.0000280579.04974.c0

Jozwiak, S., Kotulska, K., Wong, M., & Bebin, M. (2020). Modifying genetic epilepsies - Results from studies on tuberous sclerosis complex. *Neuropharmacology*, *166*, 107908. https://doi.org/10.1016/j.neuropharm.2019.107908

Jurca, A. A., Jurca, A. D., Petchesi, C. D., Bembea, D., Jurca, C. M., Severin, E., Jurca, S., & Vesa, C. M. (2025). Tuberous Sclerosis Complex: New Insights into Pathogenesis and Therapeutic Breakthroughs. *Life (Basel)*, *15*(3). https://doi.org/10.3390/life15030368

Kashii, H., Kasai, S., Sato, A., Hagino, Y., Nishito, Y., Kobayashi, T., Hino, O., Mizuguchi, M., & Ikeda, K. (2023). Tsc2 mutation rather than Tsc1 mutation dominantly causes a social deficit in a mouse model of tuberous sclerosis complex. *Hum Genomics*, *17*(1), 4. https://doi.org/10.1186/s40246-023-00450-2

Khaparde, A., Patra, R., Roy, S., Babu, G. R. S., & Ghosh, A. (2025). Improving AAV Production Yield and Quality for Different Serotypes Using Distinct Processing Methods. *ACS Omega*, *10*(22), 22657–22670. https://doi.org/10.1021/acsomega.4c10900

Kim, S. Y. (2025). Insights into Tuberous Sclerosis Complex : From Genes to Clinics. *J Korean Neurosurg Soc*, *68*(3), 321–337. https://doi.org/10.3340/jkns.2025.0035

Klaft, Z. J., Duerrwald, L. M., Gerevich, Z., & Dulla, C. G. (2020). The adenosine A1 receptor agonist WAG 994 suppresses acute kainic acid-induced status epilepticus in vivo. *Neuropharmacology*, *176*, 108213. https://doi.org/10.1016/j.neuropharm.2020.108213

Klonowska, K., Giannikou, K., Grevelink, J. M., Boeszoermenyi, B., Thorner, A. R., Herbert, Z. T., Afrin, A., Treichel, A. M., Hamieh, L., Kotulska, K., Jozwiak, S., Moss, J., Darling, T. N., & Kwiatkowski, D. J. (2023). Comprehensive genetic and phenotype analysis of 95 individuals with mosaic tuberous sclerosis complex. *Am J Hum Genet*, *110*(6), 979–988. https://doi.org/10.1016/j.ajhg.2023.04.002

Lindsay, N., Runicles, A., Johnson, M. H., Jones, E. J. H., Bolton, P. F., Charman, T., & Tye, C. (2024). Early development and epilepsy in tuberous sclerosis complex: A prospective

longitudinal study. *Dev Med Child Neurol*, *66*(5), 635–643. https://doi.org/10.1111/dmcn.15765

McColl-Carboni, A., Dollive, S., Laughlin, S., Lushi, R., MacArthur, M., Zhou, S., Gagnon, J., Smith, C. A., Burnham, B., Horton, R., Lata, D., Uga, B., Natu, K., Michel, E., Slater, C., DaSilva, E., Bruccoleri, R., Kelly, T., & McGivney, J. B. t. (2024). Analytical characterization of full, intermediate, and empty AAV capsids. *Gene Ther*, *31*(5-6), 285–294. https://doi.org/10.1038/s41434-024-00444-2

McCoy, C., Dusing, M., Jerow, L. G., Winstel, G. C., Zhan, F., Rogers, J. L., Wesley, M., Otten, J. B., Danzer, S. C., & LaSarge, C. L. (2025). Focal postnatal deletion of Tsc2 causes epilepsy. *Front Mol Neurosci*, *18*, 1686023. https://doi.org/10.3389/fnmol.2025.1686023

Mendell, J. R., Al-Zaidy, S., Shell, R., Arnold, W. D., Rodino-Klapac, L. R., Prior, T. W., Lowes, L., Alfano, L., Berry, K., Church, K., Kissel, J. T., Nagendran, S., L'Italien, J., Sproule, D. M., Wells, C., Cardenas, J. A., Heitzer, M. D., Kaspar, A., Corcoran, S.,…Kaspar, B. K. (2017). Single-Dose Gene-Replacement Therapy for Spinal Muscular Atrophy. *N Engl J Med*, *377*(18), 1713–1722. https://doi.org/10.1056/NEJMoa1706198

Mitchell, R. A., Mitchell, M., & Williams, K. (2022). The autism spectrum disorder phenotype in children with tuberous sclerosis complex: A systematic review and meta-analysis. *Dev Med Child Neurol*, *64*(10), 1214–1229. https://doi.org/10.1111/dmcn.15307

Moavero, R., Benvenuto, A., Emberti Gialloreti, L., Siracusano, M., Kotulska, K., Weschke, B., Riney, K., Jansen, F. E., Feucht, M., Krsek, P., Nabbout, R., Jansen, A. C., Wojdan, K., Borkowska, J., Sadowski, K., Hertzberg, C., Hulshof, H., Samueli, S., Benova, B.,…Curatolo, P. (2019). Early Clinical Predictors of Autism Spectrum Disorder in Infants with Tuberous Sclerosis Complex: Results from the EPISTOP Study. *J Clin Med*, *8*(6). https://doi.org/10.3390/jcm8060788

Nabbout, R., Belousova, E., Benedik, M. P., Carter, T., Cottin, V., Curatolo, P., Dahlin, M., L, D. A., d'Augères, G. B., de Vries, P. J., Ferreira, J. C., Feucht, M., Fladrowski, C., Hertzberg, C., Jozwiak, S., Lawson, J. A., Macaya, A., Marques, R., O'Callaghan, F.,…Kingswood, J. C. (2019). Epilepsy in tuberous sclerosis complex: Findings from the TOSCA Study. *Epilepsia Open*, *4*(1), 73–84. https://doi.org/10.1002/epi4.12286

Northrup, H., Aronow, M. E., Bebin, E. M., Bissler, J., Darling, T. N., de Vries, P. J., Frost, M. D., Fuchs, Z., Gosnell, E. S., Gupta, N., Jansen, A. C., Jóźwiak, S., Kingswood, J. C., Knilans, T. K., McCormack, F. X., Pounders, A., Roberds, S. L., Rodriguez-Buritica, D. F., Roth, J.,…Krueger, D. A. (2021). Updated International Tuberous Sclerosis Complex Diagnostic Criteria and Surveillance and Management Recommendations. *Pediatr Neurol*, *123*, 50–66. https://doi.org/10.1016/j.pediatrneurol.2021.07.011

Ogórek, B., Hamieh, L., Hulshof, H. M., Lasseter, K., Klonowska, K., Kuijf, H., Moavero, R., Hertzberg, C., Weschke, B., Riney, K., Feucht, M., Scholl, T., Krsek, P., Nabbout, R., Jansen, A. C., Benova, B., Aronica, E., Lagae, L., Curatolo, P.,…Kwiatkowski, D. J. (2020). TSC2 pathogenic variants are predictive of severe clinical manifestations in TSC infants: results of the EPISTOP study. *Genet Med*, *22*(9), 1489–1497. https://doi.org/10.1038/s41436-020-0823-4

Osman, M. F., Hadid, F., Ben Omran, T., Aden, M., Al-Maadid, F., Altaraqji, S., Mohamed, K., & Benini, R. (2024). Neuropsychiatric profile in tuberous sclerosis complex patients with epilepsy. *Front Pediatr*, *12*, 1436061. https://doi.org/10.3389/fped.2024.1436061

Parthasarathy, S., Mahalingam, R., Melchiorre, J., Harowitz, J., & Devinsky, O. (2021). Mortality in tuberous sclerosis complex. *Epilepsy Behav*, *121*(Pt A), 108032. https://doi.org/10.1016/j.yebeh.2021.108032

Pentz, R., Sham, L., Zak, M., Muir, K., Trinari, E., Donner, E. J., Nouri, M. N., & Whitney, R. (2025). Mortality in Tuberous sclerosis Complex: Current understandings. *Eur J Paediatr Neurol*, *58*, 83–91. https://doi.org/10.1016/j.ejpn.2025.08.002

Prabhakar, S., Goto, J., Zhang, X., Sena-Esteves, M., Bronson, R., Brockmann, J., Gianni, D., Wojtkiewicz, G. R., Chen, J. W., Stemmer-Rachamimov, A., Kwiatkowski, D. J., & Breakefield, X. O. (2013). Stochastic model of Tsc1 lesions in mouse brain. *PLoS One*, *8*(5), e64224. https://doi.org/10.1371/journal.pone.0064224

Prabhakar, S., Zhang, X., Goto, J., Han, S., Lai, C., Bronson, R., Sena-Esteves, M., Ramesh, V., Stemmer-Rachamimov, A., Kwiatkowski, D. J., & Breakefield, X. O. (2015). Survival benefit and phenotypic improvement by hamartin gene therapy in a tuberous sclerosis mouse brain model. *Neurobiol Dis*, *82*, 22–31. https://doi.org/10.1016/j.nbd.2015.04.018

Pun, R. Y., Rolle, I. J., Lasarge, C. L., Hosford, B. E., Rosen, J. M., Uhl, J. D., Schmeltzer, S. N., Faulkner, C., Bronson, S. L., Murphy, B. L., Richards, D. A., Holland, K. D., & Danzer, S. C. (2012). Excessive activation of mTOR in postnatally generated granule cells is sufficient to cause epilepsy. *Neuron*, *75*(6), 1022–1034. https://doi.org/10.1016/j.neuron.2012.08.002

Rosengren, T., Nanhoe, S., de Almeida, L. G. D., Schönewolf-Greulich, B., Larsen, L. J., Hey, C. A. B., Dunø, M., Ek, J., Risom, L., Nellist, M., & Møller, L. B. (2020). Mutational analysis of TSC1 and TSC2 in Danish patients with tuberous sclerosis complex. *Sci Rep*, *10*(1), 9909. https://doi.org/10.1038/s41598-020-66588-4

Rosset, C., Netto, C. B. O., & Ashton-Prolla, P. (2017). TSC1 and TSC2 gene mutations and their implications for treatment in Tuberous Sclerosis Complex: a review. *Genet Mol Biol*, *40*(1), 69–79. https://doi.org/10.1590/1678-4685-gmb-2015-0321

Samanta, D. (2024). Evolving treatment strategies for early-life seizures in Tuberous Sclerosis Complex: A review and treatment algorithm. *Epilepsy Behav*, *161*, 110123. https://doi.org/10.1016/j.yebeh.2024.110123

Serganova, I., & Blasberg, R. G. (2019). Molecular Imaging with Reporter Genes: Has Its Promise Been Delivered? *J Nucl Med*, *60*(12), 1665–1681. https://doi.org/10.2967/jnumed.118.220004

Singh, A., Hadjinicolaou, A., Peters, J. M., & Salussolia, C. L. (2023). Treatment-Resistant Epilepsy and Tuberous Sclerosis Complex: Treatment, Maintenance, and Future Directions. *Neuropsychiatr Dis Treat*, *19*, 733–748. https://doi.org/10.2147/ndt.S347327

Specchio, N., Di Micco, V., Scheper, M., Aronica, E., & Curatolo, P. (2025). Mechanistic strategies for secondary prevention of developmental and epileptic encephalopathy in children with tuberous sclerosis complex. *EBioMedicine*, *116*, 105740. https://doi.org/10.1016/j.ebiom.2025.105740

Specchio, N., Nabbout, R., Aronica, E., Auvin, S., Benvenuto, A., de Palma, L., Feucht, M., Jansen, F., Kotulska, K., Sarnat, H., Lagae, L., Jozwiak, S., & Curatolo, P. (2023). Updated clinical recommendations for the management of tuberous sclerosis complex associated epilepsy. *Eur J Paediatr Neurol*, *47*, 25–34. https://doi.org/10.1016/j.ejpn.2023.08.005

Sugiura, H., Yasuda, S., Katsurabayashi, S., Kawano, H., Endo, K., Takasaki, K., Iwasaki, K., Ichikawa, M., Kobayashi, T., Hino, O., & Yamagata, K. (2015). Rheb activation disrupts

spine synapse formation through accumulation of syntenin in tuberous sclerosis complex. *Nat Commun*, *6*, 6842. https://doi.org/10.1038/ncomms7842

Tavazoie, S. F., Alvarez, V. A., Ridenour, D. A., Kwiatkowski, D. J., & Sabatini, B. L. (2005). Regulation of neuronal morphology and function by the tumor suppressors Tsc1 and Tsc2. *Nat Neurosci*, *8*(12), 1727–1734. https://doi.org/10.1038/nn1566

Thiele, E. A. (2010). Managing and understanding epilepsy in tuberous sclerosis complex. *Epilepsia*, *51 Suppl 1*, 90–91. https://doi.org/10.1111/j.1528-1167.2009.02458.x

Tian, X., Glass, J. E., Kwiatkowski, D. J., Towbin, A. J., Li, Y., Sund, K. L., Krueger, D. A., Franz, D. N., McCormack, F. X., & Gupta, N. (2021). Lymphangioleiomyomatosis Association with Underlying Genotype in Patients with Tuberous Sclerosis Complex. *Ann Am Thorac Soc*, *18*(5), 815–819. https://doi.org/10.1513/AnnalsATS.202008-911OC

Uwe Schmidt, Martin Weigert, Coleman Broaddus, and Gene Myers. Cell Detection with Star-convex Polygons. *International Conference on Medical Image Computing and Computer-Assisted Intervention (MICCAI)*, Granada, Spain, September 2018.

Valente, K. D., Sampaio, L. B., Vincentiis, S., Pinto, A. L. R., & Montenegro, M. A. (2025). Tuberous Sclerosis Complex: An updated in the treatment of epilepsy for early careers. *Epilepsy Behav*, *167*, 110396. https://doi.org/10.1016/j.yebeh.2025.110396

van Slegtenhorst, M., Nellist, M., Nagelkerken, B., Cheadle, J., Snell, R., van den Ouweland, A., Reuser, A., Sampson, J., Halley, D., & van der Sluijs, P. (1998). Interaction between hamartin and tuberin, the TSC1 and TSC2 gene products. *Hum Mol Genet*, *7*(6), 1053–1057. https://doi.org/10.1093/hmg/7.6.1053

Winden, K. D., Sundberg, M., Yang, C., Wafa, S. M. A., Dwyer, S., Chen, P. F., Buttermore, E. D., & Sahin, M. (2019). Biallelic Mutations in TSC2 Lead to Abnormalities Associated with Cortical Tubers in Human iPSC-Derived Neurons. *J Neurosci*, *39*(47), 9294–9305. https://doi.org/10.1523/jneurosci.0642-19.2019

Wu, Z., Yang, H., & Colosi, P. (2010). Effect of genome size on AAV vector packaging. *Mol Ther*, *18*(1), 80–86. https://doi.org/10.1038/mt.2009.255

Zeng, L. H., Xu, L., Gutmann, D. H., & Wong, M. (2008). Rapamycin prevents epilepsy in a mouse model of tuberous sclerosis complex. *Ann Neurol*, *63*(4), 444–453. https://doi.org/10.1002/ana.21331